

---

## Intraseasonal variability of nearshore productivity in the Northern Humboldt Current System: the role of coastal trapped waves

Vincent Echevin<sup>a,\*</sup>, Aurélie Albert<sup>a</sup>, Marina Lévy<sup>a</sup>, Michelle Graco<sup>b</sup>, Olivier Aumont<sup>c</sup>, Alice Piétri<sup>d</sup>, Gilles Garric<sup>e</sup>

<sup>a</sup> Laboratoire d'Océanographie et de Climatologie: Expérimentation et Analyse Numérique (LOCEAN), Institut Pierre-Simon Laplace (IPSL), UPMC/CNRS/IRD/MNHN, 4 Place Jussieu, Case 100, 75252 Paris cedex 05, France

<sup>b</sup> Instituto del MAR del PERU (IMARPE), Esquina general Gamarra y Valle, Callao, Peru

<sup>c</sup> Laboratoire de Physique des Océans (LPO), UBO/CNRS/IRD/Ifremer, Ifremer - Centre de Brest, 29280 Plouzané, France

<sup>d</sup> Helmolz Center for ocean research, Kiel, Germany

<sup>e</sup> Mercator Océan, Parc Technologique du Canal, 8-10 rue Hermès, 31520 Ramonville St-Agne, France

\*: Corresponding author : Vincent Echevin, tel.: +33 144 277 078 ; fax: +33 144 273 805 ; email address : [vech@locean-ipsl.upmc.fr](mailto:vech@locean-ipsl.upmc.fr)

---

### Abstract:

The impact of intraseasonal coastal-trapped waves on the nearshore Peru ecosystem is investigated using observations and a regional eddy-resolving physical-ecosystem coupled model. Model results show that intraseasonal variability over the period 2000–2006 represents about one fourth of the total surface chlorophyll variance and one third of the carbon export variance on the Peruvian shelf. Evidence is presented that subsurface nutrient and chlorophyll intraseasonal variability are mainly forced by the coastally trapped waves triggered by intraseasonal equatorial Kelvin waves reaching the south american coast, and propagate poleward along the Peru shore at a speed close to that of high order coastal trapped waves modes. The currents associated with the coastal waves induce an input of nutrients that triggers a subsequent phytoplankton bloom and carbon export. The impact of the local wind-forced intraseasonal variability on the ecosystem is of a similar order of magnitude to that remotely forced in the northern part of the Peru shelf on [50–90] day time scales and dominates over the entire shelf on [20–30] day time scales.

### Highlights

► Strong intraseasonal variability of near shore plankton in Peru upwelling system. ► Chlorophyll variability is driven by the intraseasonal coastally trapped waves. ► Chlorophyll anomalies propagate poleward at speed of high order CTW mode. ► Intraseasonal wind impacts mainly the northern shelf variability and at 20–30 days.

**Keywords** : Coastally trapped waves ; Upwelling dynamics ; Humboldt system ; Intraseasonal variability ; Primary productivity

## 1. Introduction

The Peru upwelling system or Northern Humboldt Current System (hereafter NHCS) holds one of the most productive ecosystems due to its unique dynamics (Bakun and Weeks, 2008). It is sustained by year-long alongshore winds blowing equatorward, which force a coastal upwelling driven by the divergence of Ekman transport. Furthermore, the shoreward decrease of the wind intensity induces a negative wind stress curl which generates an intense Ekman pumping off the central Peru shelf (Halpern, 2002, Albert et al., 2010). These mechanisms induce nearshore upwelling of nutrient-enriched coastal waters, high biological productivity and abundant fisheries (Chavez et al., 2008).

A specific feature of this system in comparison with other Eastern Boundary Upwelling Systems (EBUS) is its relative proximity to the equatorial Pacific ocean which makes it particularly sensitive to oceanic perturbations of equatorial origin. These perturbations are characterized by the eastward propagation of energetic intraseasonal Equatorial Kelvin waves (IEKW) across the tropical ocean, forced by westerly wind bursts in the western Pacific (Kessler and McPhaden, 1995, Cravatte et al., 2003). Upon reaching the coasts of Ecuador and Peru, IEKW generate poleward-propagating coastal trapped waves (hereafter CTW) (Clarke, 1983, Belmadani et al., 2012) which, in turn, may force westward-propagating Rossby waves in frequency-dependent latitude ranges (Clarke and Shi, 1991). Such Rossby waves modulate the width of the nearshore chlorophyll-rich band as the associated currents and eddies transport phytoplankton-rich coastal waters offshore (Bonhomme et al., 2007).

During the course of their poleward propagation, CTW produce vertical displacements of the pycnocline of the order of tens of meters, associated with sea level changes of a few centimeters (Leth and Middleton, 2006, Colas et al., 2008, Belmadani et al., 2012). Associated with these vertical movements, displacements of the nutricline may modulate nutrient input into the euphotic layer and impact the biological productivity of the coastal

system. Furthermore, the amplitude of IEKW and hence of CTW is modulated at interannual time scales, as during ENSO events (Mc Phaden, 1999, Lengaigne et al., 2002). During the onset of strong El Nino events (*e.g.* 1982-1983, 1997-1998), the nearshore nutricline deepens by several tens of meters along the South American coasts as far south as central Chile, leading to tremendous impacts on all trophic levels of the ecosystem (Barber and Chavez, 1983, Carr et al., 2002, Carr, 2003, Ulloa et al., 2001).

Besides the remote forcing of CTW of 60-120 day time periods, intraseasonal wind events may also induce local upwelling and force CTW in the NHCS due to alongshore gradients of wind stress or cape effects (Crépon and Richez, 1982). Such atmospheric events are partly related with meridional displacements of the mid latitude South East Pacific anticyclone (Hormazabal et al., 2002, Dewitte et al., 2011). They result in the intensification of surface winds off north ( $5^{\circ}\text{S}$ ) and central ( $15^{\circ}\text{S}$ ) Peru, at time periods near 10-25 days and 35-60 days (Stuart, 1981, Dewitte et al., 2011).

The impact of the remote and locally-forced intraseasonal variability on the nearshore biological productivity of the NHCS has been poorly investigated so far for various reasons. First, it is difficult to evaluate the regional impact of intraseasonal variability from observations. SeaWiFS satellite data long time series are relatively scarce due to the intermittent cloud cover, particularly persistent during austral winter (Chavez, 1995). Second, estimating the impact of CTW on the ecosystem from the few coastal moorings off Peru (Graco et al., 2007) and Chile (Ulloa et al. 2001) is hindered by the intrinsic chaotic variability related with ubiquitous mesoscale eddies and submesoscale filaments of the boundary current system (Penven et al., 2005, Chaigneau et al., 2009). Such dynamical features locally generate vertical displacements of the pycnocline and nutricline, which are intertwined with the CTW-forced movements of larger alongshore scale.

To investigate the impact of CTW on the low trophic levels of the ecosystem, we follow a modelling strategy and make use of previous bio-dynamical model developments focussed on surface chlorophyll variability (Echevin et al., 2008, Albert et al., 2010). Our modelling approach allows us to simulate IEKW, CTW and intraseasonal wind stress events, and investigate their impact on the biogeochemical productivity. Using these tools we characterize the remote and local intraseasonal forcing and the biological response of the upwelling system.

In the next section we describe our modelling methodology, in particular the intraseasonal physical forcing, and the observations which are used to evaluate the model's realism. Then the physical and biogeochemical model components are validated against the available observations. Several diagnostics are proposed to characterize the time scales of the biogeochemical system intraseasonal variability, the alongshore propagating patterns and their vertical structure. The transport mechanisms which drive nutrient input on the shelf during the passage of CTW are also analysed. Finally, a discussion of the results and limitations of the approach is proposed, and the main conclusions and perspectives of this work are drawn in the closing section.

## **2. Material and Methods**

### **2.1 Numerical model and configuration**

The ROMS-AGRIF (<http://roms.mpl.ird.fr/>) model is used for ocean dynamics. It solves the primitive equations in an Earth centered rotating environment, based on the Boussinesq approximation and hydrostatic vertical momentum balance. It is discretized in terrain-following vertical coordinates. A third-order, upstream-biased advection scheme allows the generation of steep tracer and velocity gradients. The horizontal grid is isotropic ( $\Delta x = \Delta y = 1/9^\circ$ , corresponding to  $\sim 13$  km in the study region) and contains  $192 \times 240$  points that

span the region between 4°N and 22°S and from 70°W to 90°W (**Figure 1**). The western boundary intersects the Galapagos Islands at 0.6°S. The bottom topography derived from the ETOPO2 database (Smith and Sandwell, 1997) has been smoothed in order to reduce potential error in the horizontal pressure gradient. The model possesses 32 stretched vertical sigma levels to obtain a vertical resolution ranging from 0.3 m to 6.25 m for the surface layer and from 0.3 m to 1086 m for the bottom layer. For more details on the dynamical model parameterizations and configuration, the reader is referred to Shchepetkin and McWilliams (2005) and to a series of paper using the same model configuration (Penven et al., 2005, Montes et al., 2010, Echevin et al., 2011).

The physical model is coupled to the PISCES (Pelagic Interaction Scheme for Carbon and Ecosystem Studies) biogeochemical model (Aumont and Bopp, 2006), which simulates the marine biological productivity, carbon and main nutrients cycling (nitrate, phosphate, silicate and iron). It includes two size classes for phytoplankton (nanophytoplankton and diatoms), zooplankton (microzooplankton and mesozooplankton) and detritus. Diatoms differ from nanophytoplankton by their need for Si, higher requirements for iron (Sunda and Huntsman, 1997), and higher half-saturation constants because of their larger size. Iron is supplied to the ecosystem by climatological atmospheric dust deposition (Tegen and Fung, 1995) and by time-constant depth-dependent sediment mobilization (Moore et al., 2004). The model structure is identical to that used in the global simulation of Aumont and Bopp (2006) and in previous NHCS regional studies (Echevin et al., 2008, Albert et al., 2010). However, some of the biological parameters used here differ from those used in previous regional and global simulations (see **Table 1**). Changes in the mean Si/C ratio (-25% with respect to values in Albert et al., 2010) and Si remineralization rate (+60%) substantially improved the fit with silicate cross-shore observations, while an increase in the nearshore source of iron improved the fit with 2000 Iron observations of Bruland et al. (2005). We also verified that moderate

changes (+/- 10%) in the grazing coefficients did not affect the phytoplankton propagative patterns characterized in section 3.2.3. Details on the comparison with observations are given in section 3.2.1.

## 2.2 Open boundary conditions (OBC)

The physical forcing introduced at the model western open boundary is a crucial ingredient to force IEKW and CTW in our simulations. The physical model is initialized and forced at the open boundaries by outputs from the ORCALIM global ocean general circulation model (OGCM) at  $1/4^\circ$  horizontal resolution (Garric et al., 2008). Different temporal sampling of the boundary conditions are used in the REF and sensitivity experiments. Three-day mean outputs of ORCALIM temperature, salinity, velocity and sea level are used in the REF simulation to fully represent IEKW over the period 2000-2006. A monthly climatology of the ORCALIM boundary forcing is also used to filter out the most part of remote intraseasonal variability in a sensitivity experiment. **Figure 2a** shows the spectrum of ORCALIM and AVISO sea level at the western boundary of the model ( $91^\circ\text{W}$ ) along the equator. The OGCM sea level is quite energetic in the intraseasonal [40-100] days, and sea level variability is slightly overestimated near  $\sim 50$  days. The sea level spectra for the climatological forcing shows that the monthly averaging (performed for the climatology) efficiently damps energy in the intraseasonal band (**Fig. 2a**).

For the biogeochemical OBC, a monthly climatology of the ORCA2-PISCES global bio-dyn coupled model at  $2^\circ$  resolution over 1992-2000 is used (L. Bopp, pers. comm.). A high frequency forcing of the nutricline movement is not available for the period 2000-2006. Note that such high frequency forcing is not necessarily required for biogeochemical boundary conditions, as vertical migrations of the nutricline are mainly forced by vertical velocity associated with the pycnocline vertical displacements.

The modelled OBC is a mixed radiative-relaxation parameterization (Marchesiello et al., 2001). An Orlanski radiative condition is imposed for the velocity and tracer variables, which are also restored towards boundary values with a time scale of 1 day (180 days, respectively) in case of inflow (outflow, respectively). The so-called Flather boundary condition is applied to the depth-integrated momentum equations. A 150 km-wide sponge layer with a viscosity of  $1000 \text{ m}^2\text{s}^{-1}$  along the open boundaries is set up to damp outgoing eddies and waves.

### 2.3 Atmospheric forcing

Quikscat daily wind stress product gridded from swath data by CERSAT (<http://www.ifremer.fr/cersat/>) is used to force the regional model at daily to interannual time scales. Spectra of alongshore wind stress (**Fig. 2b**) displays a high level of energy in the intraseasonal [30-70 days] band, particularly off south Peru ([11°S-16°S]) in the vicinity of the Paracas Peninsula where surface winds are enhanced (Dewitte et al., 2011). A Quikscat monthly climatology over the period 2000-2006, in which intraseasonal variability is damped (**Fig. 2b**), is also used in a sensitivity experiment focusing on the remotely-forced intraseasonal variability.

The ORCALIM OGCM has been forced using daily wind stress and heat fluxes from the Integrated Forecast System (IFS) operational forecast model of the European Center for Medium-Range Weather Forecasts (ECMWF) (<http://www.ecmwf.int/research/ifsdocs/>). Thus, stored three-day mean outputs of solar and net heat flux from the IFS model are used as inputs for the regional model. Furthermore, the ROMS heat flux formulation includes a relaxation term towards Reynolds daily SST (Reynolds et al., 2007), following the parameterization of Barnier et al. (1995).

Atmospheric forcing fields, physical and biogeochemical initial conditions and OBC were interpolated onto the ROMS grid using the ROMSTOOLS pre-processing package (Penven et al., 2008).

#### **2.4 Simulations characteristics**

A three-year dynamical spin-up is first performed for the dynamics using the monthly climatological forcing, to adjust the initial state to the dynamics of the regional model. Then a 10-year spin-up simulation is run for the biogeochemical model to reach a statistical steady state. Note that the mean kinetic energy of the model adjusts after three years (*e.g.* see Fig.3 in Penven et al. (2005)) while the biogeochemical spin-up is longer (not shown). The end of the spin-up simulation is used as initial state (January 1<sup>st</sup>, 2000) for the 2000-2006 reference simulation.

Three sensitivity simulations are performed. The OBCLIM simulation uses climatological OBC and intraseasonal wind stress over 2000-2006 to filter out most of the remotely-forced intraseasonal variability. The WCLIM simulation uses intraseasonal OBC over 2000-2006 and climatological wind stress to filter out wind stress intraseasonal variability. The CLIM simulation is forced by OBC and wind stress climatological forcing, and consists in a 7 year climatological run. CLIM aims at illustrating the intrinsic intraseasonal variability of the system due to the chaotic nature of the circulation allowed by the eddy-permitting model. In all simulations, the model outputs are stored every 3 days over the 2000-2006 period. **Table 2** summarizes the simulations characteristics.

#### **2.5 Data sets used for model evaluation**

AVISO satellite altimetric data (<http://www.aviso.oceanobs.com/>) in the period January 2000–December 2006 are used to evaluate the model sea level variability. Weekly data available on a  $1/3^\circ$  gridded field result from optimal interpolation of combined altimetric data from Jason-1 and ENVISAT satellites (Le Traon et al., 1998, Ducet et al., 2000).

Surface chlorophyll concentrations are provided by the SeaWiFS satellite data (<http://oceancolor.gsfc.nasa.gov/SeaWiFS/>) over the 2000–2006 period. Data are rebinned from the original  $0.0879^\circ \times 0.0879^\circ$  grid onto the  $1/9^\circ$  model grid.

Surface chlorophyll, nitrate, phosphate and silicate *in situ* concentrations off Peru collected by Instituto del Mar del Peru (IMARPE) during the period 1992–2004 along cross-shore sections at  $\sim 10$ – $25$  km resolution are also used. Filtering of the data was performed by eliminating statistical outliers. A monthly climatological product was then constructed on a  $0.5^\circ$  grid. A more detailed description of the data processing and quality control can be found in Echevin et al. [2008]. Dissolved iron measurements are available from two cross shore transects ( $8^\circ\text{S}$  and  $13^\circ\text{S}$ ) sampled during austral winter of 2000 (Bruland et al., 2005).

## 2.6 Coastal time series

Coastal time series are obtained by averaging the signals (e.g. sea level, isotherm and iso-nitrate depth, surface chlorophyll) in a 100-km wide, coastal ribbon. This data processing partly filters the shorter, meso- and submesoscale features on the NHCS shelf, without affecting the larger, alongshore spatial scale  $L$  associated with the CTW, with  $L \sim 1000$  km ( $L \sim C \cdot T$ , with  $C \sim 1$ – $2$   $\text{m}\cdot\text{s}^{-1}$  the propagation speed (Clarke and Shi, 1991) and  $T \sim 60$  days the CTW time period).

## 2.7 Spectral analysis

Band-pass filtering is performed to analyse intraseasonal variability in various frequency bands. It combines a low-pass and a high-pass Hanning filter from the Ferret software (<http://ferret.wrc.noaa.gov/Ferret/>). Cutoff frequencies are adjusted so that the signal retains more than 80% of its amplitude within the targeted bands ([50-70] days and [100-140] days).

Variance-preserving spectra of time series are calculated using Fast Fourier Transform and smoothing in the frequency domain using a Bartlett spectral window, which allows to calculate the degrees of freedom and to estimate the 95% confidence limits for the coherence-squared estimates.

## **2.8 Analysis of alongshore velocity propagation patterns**

The modelled alongshore velocity field is analysed following two different approaches to illustrate poleward propagation associated with CTW. First, the  $f$ -plane, linear, coastal trapped wave model of Brink and Chapman (1987) is used to estimate the alongshore propagation speed and the vertical structure of the different theoretical coastal trapped waves (e.g. Brink, 1982, Jordi et al., 2005). A nearshore averaged density profile and cross-shore bottom topography from the ROMS model are used as inputs for the linear model. Second, empirical orthogonal functions (EOFs) are computed over cross-shore vertical sections of alongshore current anomalies at several latitudes (8°S and 12°S), as in Belmadani et al. (2012). A band-pass filter is previously applied to the anomalies in order to extract the intraseasonal frequencies of interest. The time series associated with the principal components are then lag correlated in order to estimate the poleward propagation speed of the different modes.

## **3. Results**

### **3.1 Dynamical response**

#### **3.1.1 Evaluation of the mean state**

We provide in this subsection a brief evaluation of the vertical structure of the modelled alongshore current. Indeed, a too shallow undercurrent may lead to an overestimation of the strength of the relationship between the CTW and the vertical velocities near the coast, and impact the biogeochemical response. As described above, our model configuration is similar to that used in Penven et al. (2005), Montes et al. (2010), Echevin et al. (2011), albeit with different boundary conditions and atmospheric forcing, thus our results can be compared with these studies. **Figure 3** displays a cross-shore section of the mean alongshore flow off the Peru shelf (12°S), averaged over the 2000-2006 period. The nearshore equatorward surface current (the Peru Coastal Current, hereafter PCC) exceeds  $\sim 10 \text{ cm.s}^{-1}$ , and reduces to zero near  $\sim 40 \text{ m}$  depth. Below the PCC, the Peru Chile Undercurrent (hereafter PCUC) flows poleward with a maximum velocity of  $\sim 9\text{-}10 \text{ cm.s}^{-1}$  near 100-130 m depth. This velocity structure is similar to the one obtained by Montes et al. (2010) (see their Figure 3). The depth and intensity of the mean PCUC are also consistent with recent shipboard acoustic doppler current profilers observations, which exhibit a PCUC core of  $\sim 10\text{-}11 \text{ cm.s}^{-1}$  at  $\sim 100\text{-}150 \text{ m}$  near 12°S-15°S, albeit for a different time period (2008-2012) (Chaigneau et al., 2013). The mean thermal structure is also well captured by the model, *e.g.* the 15°C (18°C) isotherm depth is  $\sim 100 \text{ m}$  ( $\sim 50 \text{ m}$ ), while it is near  $\sim 90 \text{ m}$  ( $\sim 50 \text{ m}$ ) in climatological World Ocean Atlas (Conkright et al., 2002) observations (*e.g.* see Figure 6 in Penven et al., 2005).

### 3.1.2 Intraseasonal variability

In this section, the realism of the modelled intraseasonal variability is evaluated. The model sea level reveals a variety of intraseasonal waves that propagate in the equatorial and coastal wave guide (**Fig. 4**). The IEKW propagation speed ( $\sim 2\text{-}3 \text{ m.s}^{-1}$ ) along the equator in our model scales with the theoretical speed derived from the first baroclinic IEKW, which ranges  $\sim 2.3\text{-}2.6 \text{ m.s}^{-1}$  for time scales of  $\sim 70$  days (Cravatte et al., 2003). CTW propagate over

large portions of the coast, at a slower velocity than IEKW, depending on the time period reflecting nearshore seasonally-varying stratification. Anomalies can be clearly identified between the equator and  $\sim 14^{\circ}\text{S}$ , while they become slightly smeared south of this limit, as they are likely to be perturbed by the more intense mesoscale variability near  $15^{\circ}\text{S}$  (Chaigneau et al., 2008). **Figure 4** also reveals a remarkable interannual modulation of the intraseasonal activity, with periods of enhanced positive anomalies during the moderate El Niño events in 2002-2003 and 2006.

Comparison between the model and observed sea level anomalies along the equator and in the coastal region highlights the realism of the modelled variability (**Fig. 5**). The time series display strong variations at intraseasonal (i.e. [60-120 days]), seasonal and interannual time scales along the equator (**Fig. 5a**) and mostly at intraseasonal time scales near the coast (**Fig. 5b**). The amplitude of the modelled sea level variations is quite realistic and the signals are highly correlated during specific periods of time (e.g. during 2002 at the coast, see **Fig. 5b**).

**Figure 6** displays the eddy kinetic energy (hereafter EKE) derived from AVISO (**Fig. 6a**) and from the REF simulation (**Fig. 6b**). EKE is derived from surface geostrophic currents computed from sea level anomalies. The agreement between the EKE patterns in terms of spatial structure and intensity, both in the near-equatorial band and near the Peru coasts suggests that the equatorially-forced intraseasonal variability, as well as the mean currents driving nearshore mesoscale turbulence through baroclinic instability, are quite realistic in the model. The vertical structure of the mean alongshore current system displays a surface jet and a poleward undercurrent which are very similar to those obtained in previous model experiments, (not shown, see Penven et al., 2005, Montes et al., 2010, 2011, Echevin et al., 2011).

A map of correlation between intraseasonal band-passed filtered observed and modelled sea level is shown in **Figure 6c**. Correlations are highest (greater than 0.6) in the near-

equatorial band (3°S-5°S) and in the coastal band. Between 8°S and 14°S offshore, patches of lower ( $\sim 0.3$ ) correlation appear, likely the signature of westward propagating Rossby waves generated at the coast by the CTW (Clarke, 1983, Belmadani et al., 2012). South of 12°S, correlation decreases and becomes nonsignificant in the deep ocean as chaotic mesoscale variability differs in the model and in the real ocean.

**Figure 7** shows the nearshore sea level spectra in two distinct coastal bands for the model and observations, on northern ([6°S-11°S]) and central ([11°S-16°S]) portions of the Peruvian shelf. On the northern shelf, the model and data spectra display a peak in the [50-70] days band, with a less energetic observed signal. Furthermore, the observed sea level variability at this time scale decreases poleward, whereas the model variability is virtually unchanged. On the southern shelf, an energy peak, absent in the model, sticks out in the [80-100] days band in the observations.

## 3.2 Biogeochemical response to IEKW forcing

### 3.2.1 Evaluation of the mean state using satellite and *in situ* observations

Figure 8 compares the simulated surface chlorophyll with SeaWiFS observations. High coastal values typical of coastal upwelling ( $\sim 5-10$  mgChl.m<sup>-3</sup> in the model versus  $\sim 4-6$  mgChl.m<sup>-3</sup> in SeaWiFS) are present in a narrow ( $\sim 50$  km) coastal band, particularly in the [6°S-12°S] latitude band. The model overestimates surface chlorophyll concentrations ( $\sim 0.5-1$  mgChl.m<sup>-3</sup> versus  $\sim 0.2-0.5$  mgChl.m<sup>-3</sup> in SeaWiFS) in the offshore equatorial region [2°N-2°S]. Modelled surface fields are compared with observed cross-shore profiles of *in situ* chlorophyll and nutrients in **Figure 9**. Modelled chlorophyll values overestimate *in situ* observations by  $\sim 1-2$  mgChl.m<sup>-3</sup> at the coast, and decrease too abruptly with distance from shore. The SeaWiFS chlorophyll profile is also shown to illustrate the range of uncertainty for the nearshore satellite measurements. The modelled and observed nitrate and phosphate fields

agree within  $\pm 1 \mu\text{mol.l}^{-1}$  and  $\pm 0.3 \mu\text{mol.l}^{-1}$ , respectively, within 100 km from the coast. The model underestimates silicate concentration by  $\sim 1\text{-}2 \mu\text{mol.l}^{-1}$ . *In situ* Iron concentrations measured during the winter of 2000 (Bruland et al., 2005) fit the model values. Note that the PISCES biogeochemical parameters (see **Table 1**) and the enhanced spatial resolution ( $1/9^\circ$ ) used here lead to more realistic patterns than those shown in previous works using the same modelling platform at a lower resolution ( $1/6^\circ$ , Echevin et al., 2008, Albert et al., 2010). The patterns from the reference simulation differ little (less than 20% (resp. 10%) change in surface chlorophyll (resp. nutrients) at the coast) from those of the CLIM simulation (dashed lines in **Fig. 9**). This shows that the nonlinearities associated with intraseasonal CTW have a weak impact on the mean biogeochemical state in our simulations.

The evolution of the observed (SeaWIFs) and modelled chlorophyll on the shelf are shown for the years 2002 and 2003 in **Figure 10a**. The frequent cloud coverage on the Peru shelf introduces many gaps in the satellite time series (**Fig. 10b**), and comparison between model and satellite observations at specific locations is difficult. Thus, spatial averaging of all data available between  $6^\circ\text{S}$  and  $15^\circ\text{S}$  and within 100km from the shore is performed in the model and in the observations, in order to take into account a large number of unflagged data. A so-called “clouded-sky” model time series, obtained by spatial-averaging model chlorophyll only during real clear-sky conditions, thus with the same amount of data as the satellite time series, is also plotted for comparison.

It is clear that no resemblance between the model and observed time series can be seen in **Figure 10a**. It is noteworthy that the “clouded-sky” and the “cloud-free” model time series differ strikingly. This shows that it is particularly arduous to validate individual events of the model chlorophyll intraseasonal variability against the sparse satellite observations due to cloud coverage. However, the variance of the modelled “clouded-sky” time series ( $\sim 2.6 \text{ (mgChl.m}^{-3}\text{)}^2$  for the 2000-2006 period) scales with that derived from the SeaWIFs time series

( $\sim 2.4 \text{ (mgChl.m}^{-3}\text{)}^2$ ). Thus, despite cloud coverage, the range of modelled variability is consistent with the range of observed variability. This suggests that the strength of the chlorophyll coastal signal intraseasonal variability is well captured by the model.

### 3.2.2 Strength of intraseasonal variability

**Figure 11** displays the spectra of nearshore surface chlorophyll on the NHCS shelf for the reference and sensitivity experiments. At short time scales ([10-30] days band), energy levels from the REF and OBCLIM simulations are similar and higher than in the WCLIM simulation, showing that chlorophyll variability is mainly related to wind-forced upwelling events. The [50-70] days band peak barely sticks out in contrast with the sea level spectra (**Fig. 7**). Energy levels are comparable ( $\sim 0.01\text{-}0.02 \text{ (mgChl.m}^{-3}\text{)}^2$ ) in all four simulations in the [30-70] days band. At longer intraseasonal time scales (e.g. [70-120] days), the chlorophyll signal holds a greater share of energy ( $\sim 0.05\text{-}0.2 \text{ (mgChl.m}^{-3}\text{)}^2$ ) than in the [50-60] days band. In this time period regime, the intrinsic energy level in the CLIM simulation decreases with respect to the other simulations, showing a clear impact of the local and remote physical forcing on the chlorophyll variability. Local (wind) and remote (ondulatory) forcing provide approximately the same input of energy ( $\sim 0.05 \text{ (mgChl.m}^{-3}\text{)}^2$  at  $\sim 120$  days) to the biogeochemical system. The remotely and locally-forced signals partly add up, the spectral energy in the REF simulation being larger ( $\sim 0.1\text{-}0.2 \text{ (mgChl.m}^{-3}\text{)}^2$  at  $\sim 120$  days) than in OBCLIM and WCLIM. Overall, when averaged over a 100 km-wide coastal ribbon between  $6^\circ\text{S}$  and  $12^\circ\text{S}$ , and integrated vertically between the surface and 50 m depth, the percentage of intraseasonal variance in the entire intraseasonal band ([10-120] days) with respect to total variance reaches 25% for chlorophyll, 13% for phytoplankton, 28% for zooplankton and 30% for export. This highlights the substantial impact of intraseasonal forcing on the NHCS biological activity.

### 3.2.3 Poleward propagation of physical and biogeochemical signals

We now examine in more detail how intraseasonal variability propagates along the coastal wave guide. Time-latitude plots of physical and biogeochemical signals filtered in the [50-80] days band for the 2001-2003 period are shown in **Figure 12** for the REF simulation. Patterns of poleward propagating sea level anomalies are clearly evidenced (**Fig. 12a**). The amplitude of the sea level anomalies varies little alongshore, between the equator and 22°S. Poleward propagation of subsurface quantities, the depth of the 17°C isotherm (hereafter DT17) and the depth of the 20  $\mu\text{mol.l}^{-1}$  iso-nitrate (hereafter DN20), a proxy of the nitracline depth, are also seen (**Fig. 12b-c**). These propagations are **not** as clearly seen as in sea level variations since these isosurfaces shoal and outcrop due to intensified upwelling and mixing during the winter season. DN20 anomalies propagate poleward between the equator and ~6-8°S, the latitude of the northern extremity of the shelf (**Fig. 12b**). At times (*e.g.* in March 2002), subsurface signals propagate as far south as ~10-12°S (~14-16°S) for DN20 (DT17). Propagating chlorophyll “waves” are also seen, mainly between ~4°S and ~14°S (**Fig.12d**), the latitude range corresponding to the chlorophyll rich shelf area (**Fig.8**) and a doming nutricline (not shown). The amplitude of the propagating chlorophyll patterns is modulated seasonally: it is highest in summer and fall when nearshore chlorophyll concentration is maximum (Echevin et al., 2008). During some events (*e.g.* February 2002), the phase of DN20 and chlorophyll anomalies are opposed, which suggest that positive chlorophyll anomalies are associated with shoaling of the nutricline. Propagative signals are also seen in other intraseasonal bands ([90-120] days and [20-30] days) (not shown).

Poleward propagation of chlorophyll is also seen on raw, unfiltered surface maps (**Fig. 13**). The situation during late summer-early fall of 2005 is shown as an example. On February 20<sup>th</sup>, a negative anomaly of ~3-5  $\text{mgChl.m}^{-3}$  appears on the Peru northern shelf (6°S-8°S). It is

blurred at specific locations (*e.g.* near 8°S, 12°S) by chlorophyll-rich filaments extending offshore. By March 10<sup>th</sup>, the negative anomaly has reached the southern part of the shelf [12°S-14°S]. On April 1<sup>st</sup>, a positive anomaly of ~5-10 mgChl.m<sup>-3</sup> reaches the northern shelf. This intense, patchy signal propagates poleward and triggers large filaments detaching from the coast.

The propagation speeds of the patterns shown in **Figure 12** are estimated using lag times and alongshore distances obtained for maximum correlations between the band-pass filtered coastal signals at various latitudes (from 6°S to 16°S (resp. 0°S to 12°S) every two degrees of latitude for chlorophyll and sea level (resp. DT17 and DN20)). This method has been used by Clarke and Ahmed (1999) to estimate sea level propagation speed off Peru. After retaining only the correlations larger than 0.2, we evaluated the propagation speed for each variable using a least square fit. Poleward wave speeds of 2.48 +/- 0.40 m.s<sup>-1</sup> for sea level, 1.03 +/- 0.16 m.s<sup>-1</sup> for DT17, 1.05 +/- 0.11 m.s<sup>-1</sup> for DN20, and 0.45 +/- 0.07 m.s<sup>-1</sup> for chlorophyll were obtained (**Table 3**).

Further evidence of the poleward propagation and vertical structure of CTW is now assessed from two different methods. First, we performed an EOF decomposition of the intraseasonal alongshore current at two latitudes (8°S, 12°S) following Belmadani et al. (2012). The first, second and third modes at 8°S (12°S) represent respectively 42.8% (43.4%), 21.7% (26.4%) and 11.7% (10.8%) of the band-passed intraseasonal variance. The vertical structure of the modes at 8°S is shown in **Figs. 14a-c**. EOF modes at 12°S present similar spatial patterns (not shown) and the associated time series at 8°S and 12°S are significantly lag-correlated, showing a poleward propagation of the statistical modes. Using the time lag at maximum correlation and the alongshore distance between the two sections, we estimated a propagation speed of 1.9 m.s<sup>-1</sup>, 0.9 m.s<sup>-1</sup>, 0.4 m.s<sup>-1</sup> for the first three EOF modes (**Table 3**). Using the same method with a lower resolution ROMS model (1/6°) over a different time

period (1992-2000), Belmadani et al. (2012) obtained roughly the same percentage of variance for the first three EOF modes as in our analysis (**Table 3**). Moreover, the poleward propagation speed for their first EOF mode between 5°S and 10°S was  $\sim 2.6 \text{ m.s}^{-1}$ , thus larger than in our case. Note that the time period in their study included the strong 1997-1998 El Nino event, which modifies the stratification and may change the waves characteristics, and that their model had a smoother shelf and slope topography than ours due to the lower spatial resolution. The topography changes may explain the reduced propagation speed of CTW (Clarke and Ahmed, 1999) in our study.

The second method is based on the estimation of theoretical CTW using the Brink and Chapman (1987) linear model. This model allows to compute pressure and velocity CTW modes as well as alongshore propagation speeds, using a cross-shore bathymetric profile and a stratification vertical profile as inputs. We performed analyses using the ROMS model stratification and bathymetry at various latitudes (8°S, 12°S) and during different time periods over 2000-2006. The obtained alongshore velocity structures for the second, third and fourth CTW modes (**Figs. 14d-f**) bear resemblance with the EOF modes, particularly the third and fourth CTW modes. Note that the CTW modes result from an idealized model which does not take into account the strong cross-shore density gradient associated with the upwelling. The propagation speeds of the CTWs modes at 8°S are  $2.0 \text{ m.s}^{-1}$ ,  $1.2 \text{ m.s}^{-1}$ ,  $0.6 \text{ m.s}^{-1}$ . Variations of these speeds with latitude are very weak. Note that the CTW first mode obtained from the linear model (not shown) is much faster ( $4.1 \pm 0.2 \text{ m.s}^{-1}$ ) than the other modes. The propagation speeds estimated with the different methods are listed in **Table 3**.

The sea level propagation speed ( $\sim 2.5 \pm 0.4 \text{ m.s}^{-1}$ ) is close but slightly larger than that obtained for the dominant EOF coastal mode ( $\sim 1.9 \text{ m.s}^{-1}$ ) and for the CTW second linear mode ( $\sim 2.0 \text{ m.s}^{-1}$ ). The slower propagation speed of subsurface quantities ( $\sim 1 \text{ m.s}^{-1}$  for DT17 and DN20) and results from the EOF analysis suggest that slower CTW modes, with virtually

no signature on sea level (**Fig.12**) are also present. Our estimate of propagation speed for the CTW third mode ( $\sim 1.2 \text{ m.s}^{-1}$ ) is close to the DN20 and DT17 wave speeds, while the CTW fourth mode value ( $\sim 0.6 \text{ m.s}^{-1}$ ) is close to the chlorophyll propagation speed ( $\sim 0.45 \text{ m.s}^{-1}$ ). Note that the linear model of Brink and Chapman (1987) does not take into account alongshore variations in stratification, bottom friction, the impact of the mean flow, and that these processes may modify the waves speed (Clarke and Ahmed, 1999). In conclusion, our results show a fast poleward propagation of sea level and a slower propagation of subsurface isotherms, nutricline depth, and surface chlorophyll. Our EOF analysis demonstrates that alongshore velocity structures also propagate, at speeds consistent with those of higher order CTW modes.

#### 3.2.4 Mechanisms driving intraseasonal variability

The link between vertical displacements of the nutricline and the biogeochemical response is illustrated by showing the cross-shore vertical structure of the nitrate field during a wave passage, as for instance during Fall 2005 (**Fig. 15**). Alongshore current anomalies (with respect to the model climatology) and tracer fields were averaged along the coast between  $7^{\circ}\text{S}$  and  $13^{\circ}\text{S}$  in order to smooth out the signature of nearshore mesoscale eddies and filaments (see Colas et al., 2008 and Echevin et al., 2011 for similar figures). A downwelling (i.e. associated with a deepening pycnocline) CTW in March 2005 is characterized by a weak ( $\sim 2 \text{ cm.s}^{-1}$ ) surface equatorward jet and a strong poleward current composed of three distinct cores of  $\sim 7\text{-}12 \text{ cm.s}^{-1}$  (**Fig.15a**). The  $5 \mu\text{mol.l}^{-1}$  nitrate isoline marking the vertical limit of the nutrient-enriched region reaches the surface at  $\sim 20 \text{ km}$  from the coast, and the chlorophyll structure exhibits a subsurface maximum near  $\sim 10\text{m}$  depth. In the case of an upwelling CTW, the surface current anomaly is reversed, showing an equatorward coastal jet of  $\sim 5\text{-}20 \text{ cm.s}^{-1}$  reaching  $30 \text{ m}$  depth (**Fig.15b**). Subsurface nitrate-replete waters have been upwelled as

shown by the nitrate enrichment in the coastal zone. The nutrient-replete coastal region (delimited by the  $5 \mu\text{mol.l}^{-1}$  nitrate isoline) has widened to  $\sim 120$  km. In addition, the nearshore phytoplankton biomass volume (*e.g.* the sea water volume with a chlorophyll concentration greater than  $3 \text{ mgChl.m}^{-3}$ ) has increased significantly. Note that the chlorophyll variability observed during the passage of such waves resulted from a net biomass variation in the nearshore domain, and not from a spatial redistribution of biomass due to vertical mixing and advection.

We now investigate the physical mechanisms driving the chlorophyll intraseasonal variability. Phytoplankton blooms are triggered by inputs of macro (nitrate, phosphate, silicate) and micro-nutrients (iron in PISCES model) into the euphotic layer, each of them having a specific spatial distribution. In contrast with results from previous modelling studies in the NHCS (Echevin et al., 2008, Albert et al., 2010), nitrate rather than iron is the main limiting nutrient in the nearshore euphotic layer in the present simulations (not shown). Thus, the nitrate fluxes driven by the CTW-associated anomalous currents are responsible for the productivity changes. To further investigate this hypothesis, the nitrate fluxes into a box encompassing the peruvian shelf are estimated. This box is made of four faces (**Fig. 1**): two 100km-wide, 50m-deep faces perpendicular to the coast at  $6^\circ\text{S}$  and  $16^\circ\text{S}$ , one located 100 km from the coast roughly parallel to the coastline, and a flat bottom at 50m depth. The zonal, meridional, vertical advective and vertical diffusion fluxes are computed online during the model integration and averaged within the coastal box (note that explicit horizontal diffusion is nul in the ROMS model as an upstream-biased advection scheme is used). Each of these terms is then band-pass-filtered in the [30-90] days time period.

The relation between total nitrate input and primary productivity is conformed by the high correlation ( $\sim 0.6$  with a 15 days time lag over 2000-2006) between phytoplankton biomass and nitrate flux in the coastal box. This time lag corresponds roughly to one quarter of the

wave time period ( $T \sim 60$  days), and is thus consistent with the relation  $\partial_t PHY = f\_NO3$ , with  $PHY$  the phytoplankton concentration and  $f\_NO3$  the total flux of nitrate into the coastal box, as the time derivative introduces a phase difference of  $T/4$ . Similar results are obtained for the [100-140] days band: the correlation is 0.37 when nitrate input leads phytoplankton concentration with a time lag of  $\sim 25$  days ( $\sim T/4$ ).

**Figure 16** displays the different physical terms (horizontal and vertical advection, total advection, vertical mixing) of the nitrate budget in the coastal box. Results are shown for the year 2005 as an example. Horizontal and vertical advection are of the same order of magnitude, have opposite signs and largely compensate each other, whereas entrainment of nutrients in the surface layer through vertical mixing is almost an order of magnitude lower. The total flux of nitrate into the box is dominated by advection processes. It is actually the sum of the horizontal and vertical fluxes which contributes to the total flux, as neither of these two terms are correlated with the total flux. Moreover, it is interesting to note that the vertical mixing flux is correlated ( $\sim 0.43$ ) with the total flux with a time lag of  $\sim 15$  days.

In conclusion, the shoaling/deepening of the nutricline, as well as the horizontal currents associated with the waves induce a nutrient flux in and out of the euphotic layer, which impacts primary production. A schematic shown in **Figure 17** summarizes these mechanisms.

### 3.2.5 Wind-forced versus remotely-forced intraseasonal variability

NHCS nearshore wind stress variability contains a significant part of energy at intraseasonal time scales (Dewitte et al., 2011), particularly in the [30-60] days band (**Fig. 2b**). Such atmospheric variability may either enhance or compensate the upwelling associated with the remotely-forced CTW through two mechanisms. On the one hand, coastal upwelling events can be generated locally by equatorward wind events. Wind-forced CTW may also be triggered by gradients of wind stress or by cape effects at specific locations of the shore

(Crépon and Richez, 1982). On the other hand, IEKW are also forced by the intraseasonal wind variability in the eastern equatorial region between the Galapagos archipelago ( $\sim 90^\circ\text{W}$ ) and the coast of Ecuador ( $\sim 81^\circ\text{W}$ ). These IEKW may also generate CTW when they reach the coast.

The impact of local intraseasonal wind variability is estimated by analysing in more details the WCLIM and OBCLIM simulation. The correlation between OBCLIM and AVISO sea level is not significant along the coast (**Fig. 6d**), which shows that the locally-forced CTW (with a sea level signature, likely the first mode) are weak in comparison with those remotely forced by the IEKW from the central and western Pacific. Nevertheless, poleward propagating patterns of chlorophyll also appear in the OBCLIM simulation. A comparison of the latitude-time diagrams is shown for a short time period (January 2005 -July 2005) in **Figure 18**. As expected, chlorophyll waves are more intense in the reference experiment (**Fig. 18a**). The chlorophyll anomalies are visible at any latitude along the coast and propagate further south than in the other experiments. Interestingly, patterns in REF and WCLIM (resp. OBCLIM) are coherent mainly south of  $\sim 6^\circ\text{S}$  (resp. north of  $\sim 10^\circ\text{S}$ ). This suggests that the IEKW-forced CTW signature on surface chlorophyll emerges in the southern shelf, whereas the locally wind-forced CTW impact mainly the northern coast and shelf. It is interesting to note that the remote and local forcings are consistent with one another during specific events (e.g. in the case of the positive anomaly reaching  $18^\circ\text{S}$  in April-May 2005, **Fig. 18a**) in the sense that the wind-forced and IEKW-forced chlorophyll waves roughly add up linearly to reconstitute the total signal from the REF experiment. Note that episodic events of poleward propagation are also evidenced along the northern Peru shore (e.g.  $[0^\circ\text{S}-8^\circ\text{S}]$  in early 2005, **Fig. 18d**) in the CLIM experiment. Thus, despite the absence of intraseasonal IEKW and wind forcing, unforced disturbances due to current instabilities also trigger a propagating biological

response in the coastal wave guide. As expected, the propagating signal in CLIM is not in phase with that in the REF, WCLIM and OBCLIM experiments.

In conclusion, results from the sensitivity experiments show that local wind variability in the NHCS generates CTW which impact chlorophyll variability mostly in the northern part of shelf (4°S-8°S). These locally-forced CTW reinforce the CTW triggered by IEKW forced by the westerly wind bursts in the western and central equatorial Pacific region, which propagate and modulate the biological signal over the whole peruvian shelf.

#### 4. Discussion

Our results highlight the poleward propagation chlorophyll waves at a speed ( $\sim 0.4 \text{ m.s}^{-1}$ ) slower than that of subsurface quantities ( $\sim 1 \text{ m.s}^{-1}$  for the 17°C isotherm and 20 $\mu\text{mol.l}^{-1}$  nitrate iso-surface). We now propose different mechanisms to explain this slower propagation. The response of the ecosystem to a CTW occurs at two different time scales. In the case of an upwelling CTW, the passing wave first triggers a bloom by uplifting the nutricline and fluxing nutrients into the euphotic layer. Meanwhile, the associated equatorward alongshore current intensifies the surface equatorward flow (**Fig. 15b**). Following the bloom, the anomalous surface chlorophyll patterns are thus advected equatorward at the velocity ( $\sim 0.1\text{-}0.3 \text{ m.s}^{-1}$ ) of the surface current and offshoreward by the Ekman flow. The combining of these alongshore displacements in opposite directions, may result in a slow poleward propagation of the chlorophyll signal. Note that the mean equatorward flow reduces to zero at  $\sim 40 \text{ m}$  depth (**Fig.3**), thus equatorward advection would not affect the subsurface signals (DT17 and DN20) as much as surface chlorophyll. Another hypothesis is the potential role played by the slowest CTW mode. Indeed, we have evidenced the presence of a EOF mode propagating poleward at  $\sim 0.4 \text{ m.s}^{-1}$ , and the existence of a CTW linear mode propagating at  $\sim 0.6 \text{ m.s}^{-1}$  (**Figs 14c-f and Table 3**). It is possible that the latter, which presents more spatial variability

in the surface layer than the other modes, would impact surface tracers (phytoplankton) more strongly.

Non linear dynamics may also perturb the poleward propagation of the surface signal. Indeed, coastal current instabilities generate mesoscale meanders, eddies and filaments. CTW also generate eddies near specific coastal locations in upwelling system (*e.g.* Leth and Middleton, 2006, for the Chilean part of the HCS). These structures, which form within ~50-100 km from the coast, are advected alongshore by the coastal current before detaching from the coast and propagating offshoreward. The chlorophyll anomalies are thus stirred by these mesoscale structures, which blurs the propagating signal. Besides, the response of the ecosystem to the nutrient flux into the euphotic layer varies in time and space because of the different environmental characteristics (temperature, light conditions, limitation level, changing depth of the nutricline), adding to the blurring effect.

A major finding of our study is the net effect of CTW on the ecosystem, in comparison with the impact of other types of waves in the open ocean. Previous works focussing on westward-propagating chlorophyll waves (Cipollini et al., 2001, Killworth et al., 2004, Dandonneau et al., 2003) have debated whether the associated perturbations induce a nutrient input into the euphotic layer and a subsequent phytoplankton bloom, or whether their action on the ecosystem consists in modifying pre-existing chlorophyll gradients through physical processes such as advection and mixing. In the NHCS, Bonhomme et al. (2007) used a simple conceptual model to show that the westward propagation of chlorophyll anomalies away from the Peru coasts at intraseasonal time scales was due to offshore advection of chlorophyll anomalies by Rossby-wave related mesoscale structures. Here CTW have a different impact on the coastal ecosystem: they enrich or deplete the coastal zone of nutrients, which modulates primary production and carbon export to the deep coastal ocean.

The intraseasonal variability documented here is typical of other EBUS also under the influence of intraseasonal equatorially-forced CTW and atmospheric variability, such as the southern HCS off Chile (Hormazabal et al., 2002), the California system (Bane et al., 2007) and the west African upwelling system (Polo et al., 2007, Lathuilière et al., 2008). In contrast with these EBUS, the NHCS is particularly prone to the influence of IEKW variability owing to a proximity with the equatorial region and a smooth coastline, which makes it an efficient wave guide for equatorial perturbations. More modelling studies are needed to investigate whether the mechanisms evidenced in this region would be relevant in other EBUS.

This study also has some limitations. The first one is the investigated time period (2000-2006) constrained by the availability of realistic wind forcing (Quikscat), OGCM output and SeaWIFs data. Note that none of the intense interannual ENSO events are included in this time period. Modulation of the IEKW activity occurs at interannual time scales (Dewitte et al., 2008), and downwelling CTW are particularly intense during the onset of ENSO events (Ulloa et al., 2001, Colas et al., 2008). Studying the impact of the interannual modulation of intraseasonal wave activity on coastal biological productivity, in particular during ENSO events, is reserved for future work. Another caveat is the use of monthly climatological boundary conditions for the biogeochemical tracers. This implies that only the intraseasonal variations of the nutricline depth driven by the boundary-forced pycnocline depth variations are represented in our simulations. Moreover, such OBC formulation generates an adjustment near the model open boundaries where the nutricline and thermocline depths do not vary in phase. This artefact may partially induce a spurious injection of nutrients into the wrong water masses near the open boundaries. Furthermore, the intraseasonal variability of the biogeochemical system could be underestimated due to the lack of intraseasonal variability in the nutrient OBC. The impact of intraseasonal nutrients boundary forcing on the regional biogeochemical system will be investigated in future work, when global or basin-scale

coupled simulations with a realistic equatorial intraseasonal variability shall become available.

As previously mentioned, nitrate limitation of primary production is prominent in the coastal range in the numerical experiments presented here. This differs from results found in previous studies (Echevin et al., 2008, Albert et al., 2010) where iron was found to be the main limiting nutrient. This shift is due to the increased iron input from sediments in the present simulations (see **Table 1**), which stimulated primary productivity and macro-nutrient consumption. However, the range of macro- and micro-nutrient concentrations off Peru remain uncertain. *In situ* subsurface nitrate measurements are relatively scarce, and few of these observations have been included in global climatologies. Moreover, one has to keep in mind that the dissolved iron data (**Fig.8e**) used to tune our model were collected during only two oceanographic cruises in 2000 (Bruland et al., 2005). However, the present results do not depend on the structure of the biogeochemical model. A sensitivity simulation using the same biogeochemical parameterizations as in Albert et al. (2010) (see **Table 1**) was performed to test the model under iron limitation. The resulting modelled surface chlorophyll is underestimated by  $\sim 2 \text{ mgChl.m}^{-3}$  at the coast, and the nitrate and phosphate fields are overestimated by  $\sim 4 \text{ }\mu\text{mol.l}^{-1}$  and by  $\sim 0.2 \text{ }\mu\text{mol.l}^{-1}$  (not shown) with respect to the *in situ* data profiles (**Fig. 8**). The response of the biogeochemical system to CTW is similar to that in the reference experiment, even though the surface variability is controlled by the advective flux of iron. Hence, the basic transport mechanism evidenced here, *i.e.* horizontal and vertical advection of subsurface nutrient into the euphotic layer associated with the passage of CTW, remains valid using a biogeochemical model with a different structure.

## 5. Conclusions and perspectives

The intraseasonal variability of the HCS coastal chlorophyll surface concentration was studied using a regional eddy-resolving coupled physical-ecosystem model and observations for the period 2000-2006. The intraseasonal variability of the dynamical solution is very realistic compared to sea level observations from altimetry. Due to the paucity of chlorophyll satellite data caused by cloud coverage and lack of *in situ* time series at intraseasonal time scales, only the model mean state could be evaluated with climatological observations. Given the satisfactory level of realism of the mean state, the model is used to document the chlorophyll variability and investigate the main driving mechanisms at intraseasonal time scales.

The intraseasonal variability is characterized by the poleward propagation of coastal disturbances triggered by coastal trapped waves, which are mainly forced by intraseasonal equatorial Kelvin waves originating from the equatorial Pacific at time scales of [60-70] days and [100-120] days. Propagation speed for sea level disturbances is faster ( $\sim 2.5 \text{ m.s}^{-1}$ ) than for thermocline/nutricline depth ( $\sim 1 \text{ m.s}^{-1}$ ) and surface chlorophyll ( $\sim 0.4 \text{ m.s}^{-1}$ ), which can be explained in terms of slow, high order CTW modes. A nitrate budget in the shelf zone shows that both horizontal and vertical advection of nutrients associated with the waves passage are the key mechanisms triggering primary productivity in the surface layer. Wind-forced variability dominates at shorter intraseasonal time scales ([20-30] days). Sensitivity experiments show that the impact of local intraseasonal wind events on the ecosystem is substantial off northern Peru, but of a lesser order of magnitude with respect to that of the remotely forced CTW. Documenting the impact of coastal waves on key environmental parameters such as oxygen subsurface concentrations (Bertrand et al., 2010) and higher trophic levels of the ecosystem will be the subject of future work.

### Acknowledgements

Model simulations were computed using the NEC-SX8 Brodie , IBM cluster Vargas supercomputers from IDRIS (<http://www.idris.fr/>) and the PC cluster network (adonis) from LOCEAN. A. Albert was funded by a scholarship of the French Ministère de l'Education et de la Recherche and by the Peru Ecosystem Projection Scenarios (PEPS) ANR-VMCS-2008 project. Christian Ethé (IPSL) and Laurent Bopp (LSCE) are greatly acknowledged for providing outputs of the global ORCA2-PISCES coupled simulation. Pascal Terray (LOCEAN) is acknowledged for providing spectral analysis tools. Gildas Cambon (LEGOS) is acknowledged for implementing the online tracer diagnostics in the ROMS-AGRIF model. Xavier Capet, Francois Colas and Alban Lazar are acknowledged for fruitful discussions. Christophe Hourdin is acknowledged for technical support with ROMS-PISCES modelling. Four anonymous reviewers are acknowledged for their constructive and helpful comments.

### **Bibliography**

- Albert, A., V. Echevin, M. Lévy, and O. Aumont, 2010. Impact of nearshore wind stress curl on coastal circulation and primary productivity in the Peru upwelling system, *J. Geophys. Res.*, 115, C12033, doi:10.1029/2010JC006569.
- Aumont, O., and L. Bopp, 2006. Globalizing results from ocean in situ iron fertilization studies, *Gl. Biogeochem. Cyc.*, 20 (GB2017), doi :10.1029/2005GB002591.
- Bakun, A., and S.J.Weeks , 2008. The marine ecosystem off Peru: what are the secrets of its fishery productivity and what might its future hold?, *Prog. Oceanogr.*, 79: 290-299.
- Bane, J.M., Y. Spitz, R.M. Letellier and W.T. Peterson, 2007. Jet stream intraseasonal oscillations drive dominant ecosystem variations in Oregon's summertime coastal upwelling system, *Proc. Nat. Acad. Sc.*, 104:13262-13267.

- Barber, R.T., and F.P. Chavez, 1983. Biological Consequences of El Nino, *Science*, Vol. 222, 1203-1210.
- Barnier, B., L. Siefridt, and P. Marchesiello, 1995. Thermal forcing for a global ocean circulation model using a three year climatology of ECMWF analyses, *J. Mar. Syst.*, 6, 363–380, doi:10.1016/0924-7963(94)00034-9.
- Belmadani, A., V. Echevin, B. Dewitte, and F. Colas, 2012. Equatorially forced intraseasonal propagations along the Peru-Chile coast and their relation with the nearshore eddy activity in 1992–2000: a modeling study, *J. Geophys. Res.*, 117, C04025, doi:10.1029/2011JC007848.
- Bertrand, A., M. Ballón, and A. Chaigneau, 2010. Acoustic Observation of Living Organisms Reveals the Upper Limit of the Oxygen Minimum Zone, *PLoS ONE* 5(4): e10330, 2010. doi:10.1371/journal.pone.0010330.
- Bonhomme, C., O. Aumont, and V. Echevin, 2007. Advective transport caused by intraseasonal rossby waves : a key player of the high chlorophyll variability off the Peru upwelling region, *J. Geophys. Res.*, Vol. 112, C09018, doi :10.1029/2006JC004022.
- Brink, K.H., 1982. A comparison of Long coastal trapped wave theory with observations off Peru, *J. Phys. Oceanogr.*, Vol. 12, 897-913.
- Brink, K., H., and D. C. Chapman, 1987. Programs for computing properties of coastal-trapped waves and wind-driven motions over the continental shelf and slope, Woods Hole Inst. Tech. Rep., WHOI-87-24, 122 pp.

- Bruland, K. W., E. L. Rue, G. J. Smith, and G. R. DiTullio, 2005. Iron, macronutrients and diatom blooms in the Peru upwelling regime: brown and blue waters of Peru, *Mar. Chem.*, 93, 81–103.
- Carr, M., P. Strub, A. Thomas, and J. Blanco, 2002. Evolution of 1996-1999 la Niña and el Niño conditions off the western coast of South America : a remote sensing perspective, *J. Geophys. Res.*, 107 (C12,3236). doi :10.1029/2001JC001183.
- Carr, M.-E., 2003. Simulation of carbon pathways in the planktonic ecosystem off Peru during the 1997–1998 El Niño and La Niña, *J. Geophys. Res.*, 108(C12), 3380, doi:10.1029/1999JC000064.
- Chaigneau, A., A. Gizolme and C. Grados, 2008. Mesoscale eddies off Peru in altimeter records: Identification algorithms and eddy spatio-temporal patterns, *Prog. Oceanogr.*, 79, 106-119.
- Chaigneau, A., G. Eldin, and B. Dewitte, 2009. Eddy activity in the four major upwelling systems from altimetry (1992-2007), *Progr. Oceanogr.*, 83, 117-123.
- Chaigneau, A., N. Dominguez, G. Eldin, L. Vasquez, R. Flores, C. Grados, and V. Echevin, 2013. Near-coastal circulation in the Northern Humboldt Current System: Mean characteristics and seasonal variations from SADCP data, *J. Geophys. Res.*, 118, doi:10.1002/jgrc.20328
- Cipollini, P., D. Cromwell, P. G. Challenor, and S. Raffaglio, 2001. Rossby waves detected in global ocean colour data, *Geophys. Res. Lett.*, 28, 323 – 326.
- Chavez, F., 1995. A comparison of ship and satellite chlorophyll from California and Peru, *J. Geophys. Res.*, 100 (C12), 24,855-24,862.

- Chavez, F., A. Bertrand, R. Guevara-Carrasco, P. Soler, and J. Csirke, 2008. The northern Humboldt current system: brief history, present status and a view towards the future, *Prog. Oceanogr.*, 79, 95-105.
- Clarke, A. J., 1983. The reflection of equatorial waves from oceanic boundaries, *J. Phys. Oceanogr.*, 13, 1193-1207.
- Clarke, A.J., and C. Shi, 1991. Critical frequencies at ocean boundaries, *J. Geophys. Res.*, 96, 10731-10738.
- Clarke, A. J., and R. Ahmed, 1999. Dynamics of remotely forced intraseasonal oscillations off the western coast of South America, *J. Phys. Oceanogr.*, 29, 240–258, doi:10.1175/1520-0485(1999)029<0240:DORFIO>2.0.CO;2.
- Conkright, M.E., R.A. Locarnini, H. E. Garcia, T.D. O'Brien, T.P. Boyer, C. Stephens, and J. Antonov, 2002. *World Ocean Atlas 2001: objectives, analyses, data statistics and figures [CD-ROM]*, NOAA Atlas NESDIS 42, Silver Spring, Md.
- Cravatte, S., J. Picaut, and G. Eldin, 2003. Second and first baroclinic kelvin modes in the equatorial pacific intraseasonal timescales, *J. Geophys. Res.*, 108 (C8,3266). doi:10.1029/2002JC001511.
- Crépon, M., and C. Richez, 1982. Transient upwelling generated by two-dimensional atmospheric forcing and variability in the coastline, *J. Phys. Oceanogr.*, 12:1437-1456.
- Colas, F., X. Capet, J. C. McWilliams, and A. Shchepetkin, 2008. 1997-98 El Niño off Peru: A numerical study, *Progr. Oceanogr.*, 79, 138-155.
- Conkright, M. E., R. A. Locarnini, H. E. Garcia, T. D. O. Brien, T. P. Boyer, C. Stephens, and J. I. Antonov (2002), *World ocean atlas 2001: Objective analyses, data statistics, and figures*, CD-ROM documentation, technical report, Natl. Oceanogr. Data Cent., Silver Spring, Md.

- Dandonneau, Y., A. Vega, H. Loisel, Y. Du Penhoat, and C. Menkes, 2003. Oceanic Rossby waves acting as a “hay rake” for ecosystem floating by-products, *Science*, 302, 1548 – 1551.
- Dewitte, B., S. Purca, S. Illig, L. Renault, and B. Giese, 2008. Low frequency modulation of the intraseasonal equatorial Kelvin wave activity in the Pacific Ocean from SODA: 1958-2001, *J. Climate*, 21, 6060-6069.
- Dewitte, B., S. Illig, L. Renault, K. Goubanova, K. Takahashi, D. Gushchina, K. Mosquera, and S. Purca, 2011. Modes of covariability between sea surface temperature and wind stress intraseasonal anomalies along the coast of Peru from satellite observations (2000–2008), *J. Geophys. Res.*, 116, C04028, doi:10.1029/2010JC006495.
- Ducet N., P.Y. Le Traon, G. Reverdin, 2000. Global high-resolution mapping of ocean circulation from the combination of T/P and ERS-1/2. *J. Geophys. Res.*, 105, 19,477-19,498.
- Echevin, V., O. Aumont, J. Ledesma, and G. Flores, 2008. The seasonal cycle of surface chlorophyll in the peruvian upwelling system : a modelling study, *Prog. Oceanogr.*, 79, 167-176.
- Echevin, V., F. Colas, A. Chaigneau, and P. Penven, 2011. Sensitivity of the Northern Humboldt Current System nearshore modeled circulation to initial and boundary conditions, *J. Geophys. Res.*, 116, C07002, doi:10.1029/2010JC006684.
- Garric, G., R. Bourdalle-Badie, O. Le Galloudec, C. Bricaud, C. Derval, E. Durand, and Y. Drillet, 2008. Description of the interannual experiment ORCA025-T09, 1998-2006, Annex 2 of Mercator Ocean Report n°235, 32 p.

- Graco, M., J. Ledesma, G. Flores, and M. Giron, 2007. Nutrients, oxygen and biogeochemical processes in the Humboldt upwelling current system off Peru., *Rev. peru. Biol.* , 14(1), 117-128.
- Halpern, D., 2002. Offshore Ekman transport and Ekman pumping off Peru during the 1997–1998 El Niño, *Geophys. Res. Lett.*, 29(5), 1075, doi:10.1029/2001GL014097.
- Hormazabal, S., G. Shaffer, and O. Pizarro, 2002. Tropical Pacific control of intraseasonal oscillations off Chile by way of oceanic and atmospheric pathways, *Geophys. Res. Lett.*, Vol. 29, N° 6, 1081, 10.1029/2001GL013481.
- Jordi, A., A. Orfila, G. Basterretxea, and J. Tintoré, 2005. Coastal trapped waves in the Northwestern Mediterranean, *Cont. Shelf Res.*, 25, 185-196.
- Kessler, W. S., and M. J. McPhaden, 1995. Oceanic equatorial waves and the 1991–1993 El Niño, *J. Climate*, 8, 1757–1774.
- Kessler, W., 2006. The circulation of the eastern tropical Pacific : a review, *Prog. Oceanogr.*, 69, 181-217. doi :10.1016/j.pocean.2006.03.009.
- Killworth, P. D., P. Cipollini, B. M. Uz, and J. R. Blundell, 2004. Physical and biological mechanisms for planetary waves observed in satellite-derived chlorophyll, *J. Geophys. Res.*, 109, C07002, doi:10.1029/2003JC001768.
- Lathuiliere, C., V. Echevin, and M. Levy, 2008. Seasonal and intraseasonal surface chlorophyll-a variability along the northwest African coast, *J. Geophys. Res.*, 113 (C5), p.0148-0227.
- Lengaigne, M., J.-P. Boulanger, C. Menkes, S. Masson, G. Madec, and P. Delecluse, 2002. Ocean response to the March 1997 Westerly Wind Event, *J. Geophys. Res.*, 107, 8015, doi:10.1029/2001JC000841.

- Leth, O., and J. F. Middleton, 2006. A numerical study of the upwelling circulation off central Chile: Effects of remote oceanic forcing, *J. Geophys. Res.*, 111, C12003, doi:10.1029/2005JC003070.
- Le Traon, P. Y., F. Nadal, and N. Ducet, 1998. An improved mapping method of multisatellite altimeter data, *J. Atmos. Ocean. Technol.*, 15, 522–534.
- Marchesiello, P., J.C. McWilliams, and A. Shchepetkin, 2001. Open boundary conditions for long-term integration of regional oceanic models, *Ocean Modelling*, 3, 1-20.
- McPhaden, M. J., 1999. Genesis and evolution of the 1997 – 1998 El Niño, *Science*, 283, 950 – 954.
- Montes, I., F. Colas, X. Capet, and W. Schneider, 2010. On the pathways of the equatorial subsurface currents in the eastern equatorial Pacific and their contributions to the Peru-Chile Undercurrent, *J. Geophys. Res.*, 115, C09003, doi:10.1029/2009JC005710.
- Montes, I., W. Schneider, F. Colas, B. Blanke, and V. Echevin, 2011. Subsurface connections in the eastern tropical Pacific during La Niña 1999–2001 and El Niño 2002–2003, *J. Geophys. Res.*, 116, C12022, doi:10.1029/2011JC007624.
- Moore, J. K., S. C. Doney, and K. Lindsay, 2004. Upper ocean ecosystem dynamics and iron cycling in a global three-dimensional model, *Glob. Biogeochem. Cyc.*, 18, GB4028, doi:10.1029/2004GB002220.
- Polo, I., A. Lazar, B. Rodriguez-Fonseca, and S. Arnault, 2008. Oceanic Kelvin waves and tropical Atlantic intraseasonal variability: 1. Kelvin wave characterization, *J. Geophys. Res.*, 113, C07009, doi:10.1029/2007JC004495.
- Reynolds, R. W., T. M. Smith, C. Liu, D. B. Chelton, K. S. Casey, and M. G. Schlax, 2007. Daily high-resolution blended analyses for sea surface temperature. *J. Climate*, 20, 5473-5496.

- Penven, P., V. Echevin, J. Pasapera, F. Colas and J. Tam, 2005. Average circulation, seasonal cycle and mesoscale dynamics of the peru current system : a modeling approach, *J. Geophys. Res.*, 110, C10021. doi :10.1029/2005JC002945.
- Penven P., P. Marchesiello, L. Debreu, and J. Lefèvre, 2008. Software tools for pre- and post-processing of oceanic regional simulations, *Environmental Modelling & Software*, 23, 660-662, doi:10.1016/j.envsoft.2007.07.004.
- Shchepetkin, A. F., and J. C. McWilliams, 2005. The Regional Ocean Modeling System: A split-explicit, free-surface, topography following coordinates ocean model, *Ocean Modelling*, 9, 347-404.
- Smith, W. H. F., and D. T. Sandwell, 1997. Global seafloor topography from satellite altimetry and ship depth soundings, *Science*, 277, 1957–1962.
- Sunda, W.G., and S.A. Huntsman, 1997. Interrelated influence of iron, light and cell size on marine phytoplankton growth. *Nature*, 390, 389–392.
- Tegen, I., Fung, I., 1995. Contribution to the atmospheric mineral aerosol load from
- Ulloa, O., R. Escribano, S. Hormazabal, R. A. Quiñones, R. R. González, and M. Ramos, 2001. Evolution and biological effects of the 1997–98 El Niño in the upwelling ecosystem off northern Chile, *Geophys. Res. Lett.*, 28(8), 1591–1594, doi:10.1029/2000GL011548.
- Stuart, D. W., 1981. Sea-surface temperatures and winds during JOINT II: Part II. Temporal fluctuations. *Coastal Upwelling*, 32-38., *Coastal Estuarine Sci.*, vol. 1, 529 pp., AGU, Washington, D. C., doi:10.1029/CO001.
- Tegen, I., and I. Fung, 1995. Contribution to the atmospheric mineral aerosol load from land surface modification, *J. Geophys. Res.*, 100, 18,707–18,726.

### Figure captions

**Figure 1** : ROMS model domain with northern, western and southern open boundaries. The black line marks the equatorial section followed by the equatorial Kelvin waves (EKW, red arrow) and the alongshore section followed by the coastal trapped waves (CTW, red arrow). These two sections are used in Figure 4. The blue dashed line marks a 100-km wide coastal box located on the central Peru shelf. Red circles mark two locations from which sea level is plotted (see Figure 5). Model surface chlorophyll in January 2000 (in  $\text{mgChl.l}^{-1}$ ) is shown in the background.

**Figure 2** : Spectra of (a) sea level (in  $\text{m}^2$ ) at  $[91^\circ\text{W}, 0^\circ\text{S}]$  at the open boundary of the regional model for AVISO (red dashed line), ORCALIM (red full line), a monthly climatology of ORCALIM (blue line); (b) Quikscat alongshore wind stress (in  $(\text{N.m}^{-2})^2$ ) averaged in two 100-km wide coastal bands ( $[4^\circ\text{S}-11^\circ\text{S}]$  and  $[11^\circ\text{S}-16^\circ\text{S}]$ ). Spectrum of a Quikscat monthly climatology is also shown (dashed lines). The  $[30, 70, 120]$  days time periods are marked by dashed vertical lines.

**Figure 3**: Cross-shore section of the modelled meridional velocity (shading, in  $\text{cm.s}^{-1}$ ) and temperature (contours, in  $^\circ\text{C}$ ) at  $12^\circ\text{S}$ , averaged over the 2000-2006 time period.

**Figure 4** : Time-longitude/latitude diagram of modelled sea level intraseasonal anomalies along the equator ( $91^\circ\text{W}-80^\circ\text{W}$ ) and the coast ( $0^\circ\text{S}-22^\circ\text{S}$ ). Sea level is detrended and band-pass filtered to emphasize intraseasonal anomalies. The equatorial and alongshore sections along which the sea level is plotted are shown in Figure 1.

**Figure 5 :** Intraseasonal sea level anomalies from AVISO (red line) and model (REF experiment, black line) at (a) 86°W on the equator (east of Galapagos Islands) and (b) 10°S near the coast. The two locations are marked by full red circles in Figure 1.

**Figure 6 :** Eddy kinetic energy (in  $\text{cm}^2.\text{s}^{-2}$ ) computed from (a) AVISO and (b) model (REF experiment). Correlation between intraseasonal AVISO and model sea level for (c) the REF and (d) OBCLIM experiments. Regions with non significant correlation (below 95% confidence level) are marked in white. EKE and correlations are computed over the 2000-2006 period.

**Figure 7:** Spectrum of sea level averaged in two coastal bands ([6°S-11°S] and [11°S-16°S]) for AVISO (dashed line) and model (REF simulation, full line). The [30, 70, 120] days time periods are marked by dashed vertical lines.

**Figure 8 :** Mean surface chlorophyll (in  $\text{mgChl}/\text{m}^3$ ) for (a) SeaWiFS observations and (b) model (REF experiment) for the 2000-2006 period. [0.5;1;2;3]  $\text{mgChl}/\text{m}^3$  isolines are marked by black contours.

**Figure 9 :** Cross-shore average transects for surface (a) chlorophyll (in  $\text{mgChl}.\text{m}^{-3}$ ), (b) nitrate (in  $\mu\text{mol}.\text{l}^{-1}$ ), (c) phosphate (in  $\mu\text{mol}.\text{l}^{-1}$ ), (d) silicate (in  $\mu\text{mol}.\text{l}^{-1}$ ) and (e) iron concentrations (in  $\text{nmol}.\text{l}^{-1}$ ). The transects are constructed by averaging all data alongshore between 6°S and 16°S. Profiles from the REF and CLIM simulations are marked by full and dashed black lines respectively; SeaWiFS chlorophyll is marked by a solid green line in (a) ; in situ IMARPE (in (a-d)) and Iron data (in (e)) from Bruland et al [2005] are marked by full red lines.

**Figure 10 :** (a) Surface chlorophyll (in  $\text{mgChl}/\text{m}^3$ ) averaged in a coastal box ( $\sim 0$ -100km from the coast,  $6^\circ\text{S}$ - $15^\circ\text{S}$ , see Figure 1) for the REF simulation (black line), REF simulation with cloud mask from SeaWiFs observations (blue crosses) and for SeaWiFs observations (green crosses). (b) Percentage of unflagged data in the coastal box.

**Figure 11 :** Spectrum of surface chlorophyll concentration (in  $(\text{mgChl}.\text{m}^{-3})^2$ ). Chlorophyll time series are computed by averaging nearshore values in a 100-km wide,  $[4^\circ\text{S}$ - $16^\circ\text{S}]$  coastal band. Full black, full red, dashed red and dot-dashed red lines mark REF, WCLIM, OBCLIM, CLIM simulations, respectively.

**Figure 12 :** Time-latitude diagram of (a) sea level (in m) and (b) depth of the  $2\mu\text{mol}.\text{l}^{-1}$  isonitrate (in m), (c) depth of the  $17^\circ\text{C}$  isotherm (in m), and (d) surface chlorophyll anomalies (in  $\text{mgChl}.\text{m}^{-3}$ ) for the REF experiment. All variables have been band-pass filtered in the  $[50$ - $80]$  days band and averaged in a 100-km-wide coastal band.

**Figure 13 :** Surface chlorophyll anomalies (in  $\text{mgChl}.\text{m}^{-3}$ ) during the passage of a CTW wave in austral fall of 2005.

**Figure 14 :** Alongshore velocity structure (in  $\text{cm}.\text{s}^{-1}$ ) corresponding to the (a) first, (b) second and (c) third Empirical Orthogonal Function (EOF) decomposition of the alongshore flow at  $8^\circ\text{S}$ . The velocity fields are band-pass filtered in the  $[50$ - $90]$  days band. The percentage of variance explained by each mode is also shown. The poleward propagation speed (c, in  $\text{m}.\text{s}^{-1}$ ) of each mode is computed from the maximum lagged correlation of the time series associated to the EOF modes at  $8^\circ\text{S}$  and  $12^\circ\text{S}$  (see **Table 3**). Alongshore velocity structure of

the (d) second, (e) third and (f) fourth coastal trapped wave (CTW) modes obtained with the Brink and Chapman (1987) linear model at 8°S. The mean stratification  $\rho(z)$  and bottom topography  $H(x)$  from the ROMS model are used. The propagation speed of the CTW modes are also indicated. The much faster first CTW mode is not shown (see **Table 3**).

**Figure 15 :** Vertical structure of the alongshore currents (in  $\text{cm}\cdot\text{s}^{-1}$ , color coding), nitrate (in  $\mu\text{mol}\cdot\text{l}^{-1}$ , white lines) and chlorophyll concentration (in  $\text{mgChl}\cdot\text{m}^{-3}$ , black lines). Currents and tracers fields have been averaged alongshore between 7°S and 13°S.

**Figure 16 :** Time evolution of nitrate flux terms (in  $\text{mol}\cdot\text{s}^{-1}$ ): total advection (red line), horizontal advection (black line), vertical advection (green line), vertical mixing (blue line) and total input (dashed red line). Fluxes are positive for a net input of nitrate into the coastal box sketched in Figure 1. Time series are band-pass filtered in the [50-90] days regime.

**Figure 17 :** Schematic diagram of the alongshore and vertical structure of the coastal trapped waves (CTW) and their impact on biological productivity. The fast and slow mode are shown in red and blue respectively. Horizontal currents and sea level variations associated with the waves are marked by thin horizontal arrows and full lines respectively. CTW poleward propagation is marked by thick colored arrows. The surface equatorward coastal flow is marked by full black arrows. The nutricline depth is marked by a curved black line. As CTW are generated in the equatorial region, the gravest CTW mode associated with a high sea level variability rapidly propagates poleward without displacing the nutricline. In the meantime, a slower mode with a lower sea level variability propagates slowly and generates vertical movements of the nutricline (vertical black arrows). This pumps nutrients in and out of the

surface layer, enhancing or mitigating primary productivity. The phytoplankton poleward propagation (thick green arrow) is modified by the surface equatorward flow.

**Figure 18:** Same as Figure 11d but for a selected time period (January-July 2005) and for (a) REF;(b) WCLIM; (c) OBCLIM; (d) CLIM simulations.

**Table 1 :** PISCES biogeochemical parameters and values used in the REF experiment (in bold ), compared with standard values from global model experiments (Kane et al., 2010) and previous regional simulations (Albert et al., 2010).

**Table 2 :** Simulation characteristics. Monthly climatologies are computed over the 2000-2006 time period. ORCALIM is the OGCM (at  $1/4^\circ$  resolution) operated by the Mercator-Ocean modelling group which provides initial and boundary conditions for the ROMS model. Biogeochemical initial and boundary conditions are provided by a climatology of the ORCA2-PISCES model (at  $2^\circ$  resolution). IFS is the Integrated Forecast System (IFS) of the European Center for Medium-Range Weather Forecasts (ECMWF).

**Table 3:** Poleward propagation speeds (bold, in  $\text{m}\cdot\text{s}^{-1}$ ) estimated using different methods: (top) from lag time and alongshore distance corresponding to maximum correlation of model time series at different latitudes; (middle) from the Brink and Chapman (1987) CTW linear model; (bottom) from lag time and alongshore distance (between  $8^\circ\text{S}$  and  $12^\circ\text{S}$ ) corresponding to maximum correlation of the time series associated to the EOF modes of the alongshore flow at  $8^\circ\text{S}$  and  $12^\circ\text{S}$ . The percentage of the variance explained by each mode is indicated. Values obtained by Belmadani et al. (2012) using the same method and a different model are also indicated.

PISCES Parameters	Standard value (Kane et al., 2010)	Peru value in Reference experiment and in Albert et al. (2010)	Parameter definition
Conc0	2. e - 6	-	phosphate half saturation (umolP l-1)
Conc1	10E - 6	-	phosphate half saturation for diatoms (umo P l-1)
Conc3	0.1E - 9	-	
Grosip	0.151	<b>0.06</b> (0.08)	iron half saturation for diatoms (nmo Fe l-1)
Pislope	4	3	
Pislope2	4	3	mean Si/C ratio
Excret	0.05	0.1	P - I slope for nano ((Wm-2)-1 d-1)
Excret2	0.05	0.1	P - I slope for diatoms ((Wm-2)-1 d-1)
Wsbio	3	-	excretion ratio of nano
Wsbio2	50	-	excretion ratio of diatoms
Wchl	0.001	-	POC sinking speed (m d-1)
Wchld	0.02	-	big particles sinking speed (m d-1)
Resrat	0.03	-	maximum aggregation rate for nano (d-1)
Resrat2	0.008	0.005	molC-1)
Mprat	0.01	-	Maximum aggregation rate for diatoms (d-1)
Mprat2	0.01	-	molC-1)
Grazrat	4	-	exsudation rate of zooplankton
Grazrat2	0.7	-	exsudation rate of mesozooplankton
Mzrat2	0.03	0.05	phytoplankton mortality rate (d-1)
Xprefc	1	-	diatoms mortality rate (d-1)
Xprefp	0.	-	maximal zoo grazing rate (d-1)
Xprefz	1	-	maximal mesozoo grazing rate (d-1)
Unass	0.3	-	mesozooplankton mortality rate ((umolC l-1)
Unass2	0.3	-	d-1)
Xkgraz	20. E - 6	-	zoo preference for phyto
Xkgraz2	20. E - 6	-	zoo preference for POC
Xkmort	1. E - 7	-	zoo preference for zoo
Xksil	2. E - 6	1.5E-6	nonassimilated fraction of phyto by zoo
Xksi2	3.33E - 6	4E-6	nonassimilated fraction of P by mesozoo
Xremip	0.025	-	half saturation constant for grazing (umolC l-1)
Xremik	0.3	0.2	
Xsirem	0.015	<b>0.025</b> (0.015)	half saturation constant for grazing 2
Xkdoc2	417. E - 6	-	(umolC l-1)
Xprefpoc	0.2	-	half saturation constant for mortality
Concnh4	1. E - 7	-	(umolC l-1)
Concdnh4	5. E - 7	-	half saturation constant for Si uptake
Nitrif	0.05	-	(umolSi l-1)
Epsher2	0.33	-	half saturation constant for Si/C (umolSi l-1)
Epsher	0.33	-	
Sigma1	0.6	-	rem mineralization rate of POC (d-1)
Sigma2	0.6	-	rem mineralization rate of DOC (d-1)
Zprefp	0.6	0.5	rem mineralization rate of Si (d-1)
Zprefd	0.5	-	second half - sat. of DOC rem mineralization
Chlcnm	0.033	-	(umolC l-1)
Chlcdm	0.05	-	zoo preference for POC
cmask	0.1	<b>0.5</b> (0.1)	NH4 half saturation for phyto (umol P l-1)

			NH4 half saturation for diatoms (umol P l <sup>-1</sup> ) NH4 nitrification rate (d <sup>-1</sup> ) efficiency of mesozoo growth efficiency of microzoo growth fraction of microzoo excretion as DOM - fraction of mesozoo excretion as DOM - microzoo preference for nanophyto microzoo preference for diatoms minimum Chl/C in nanophytoplankton (mgChl/mgC) minimum Chl/C in diatoms (mgChl/mgC) nearshore source input of iron (non dimensional)
--	--	--	--

**Table 1** : Biogeochemical Parameters from ROMS-PISCES, compared with standard values from global (Kane et al., 2010) and previous regional simulations (Albert et al., 2010). Values in bold mark parameter values used in the reference simulation.

ROMS-PISCES simulation	OBC forcing (ORCALIM)	Wind stress forcing (Quikscat)	Heat fluxes (IFS)
REF	3-day-mean	Daily	3-day-mean
OBCLIM	Monthly climatology	Daily	3-day-mean
WCLIM	3-day-mean	Monthly climatology	Monthly climatology
CLIM	Monthly climatology	Monthly climatology	Monthly climatology

**Table 2** : ROMS-PISCES simulation characteristics. Monthly climatologies are computed over the 2000-2006 time period.

ROMS-PISCES simulation	OBC forcing (ORCALIM)	Wind stress forcing (Quikscat)	Heat fluxes (IFS)
REF	3-day-mean	Daily	3-day-mean
OBCLIM	Monthly climatology	Daily	3-day-mean
WCLIM	3-day-mean	Monthly climatology	Monthly climatology
CLIM	Monthly climatology	Monthly climatology	Monthly climatology

**Table 2** : ROMS-PISCES simulation characteristics. Monthly climatologies are computed over the 2000-2006 time period.

Model variables	Sea level	17° C depth	20 $\mu\text{M}$ nitrate	Surface Chl
Propagation speed (in $\text{m}\cdot\text{s}^{-1}$ )	<b>2.48 +/- 0.40</b>	<b>1.03 +/- 0.16</b>	<b>1.05 +/- 0.11</b>	<b>0.45 +/- 0.07</b>
CTW linear mode n°	first	second	third	fourth
Propagation speed at 8° S	<b>4.33 +/- 0.02</b>	<b>2.02 +/- 0.01</b>	<b>1.15 +/- 0.02</b>	<b>0.59 +/- 0.01</b>
Propagation speed at 12° S	<b>3.79 +/- 0.02</b>	<b>1.64 +/- 0.01</b>	<b>1.00 +/- 0.01</b>	<b>0.54 +/- 0.01</b>
EOF Mode n°		first	second	third
Mode variance at 8° S		42.8%	21.7%	11.7%
Mode variance at 12° S		43.4%	26.4%	10.8%
Mode variance at 10° S from Belmadani et al. (2012)		55,00%	23.8%	10,00%
Maximum lag-correlation 8° S-12° S		0.53	0.14	0.29
Propagation speed estimated from the lag-correlation		<b>1, 9</b>	<b>0, 9</b>	<b>0, 4</b>

**Table 3** : Poleward propagation speeds (in bold, in  $\text{m}\cdot\text{s}^{-1}$ ) estimated using different methods: (top) from lag time and alongshore distance corresponding to maximum correlation of model variables at different latitudes. Errors are outputs of the least square estimation ; (middle) from the Brink and Chapman (1987) CTW linear model. Errors correspond to the interannual variability of the CTW speed; (bottom) from lag time and alongshore distance corresponding to maximum correlation between the time series associated to the EOF decomposition of the alongshore flow at 8°S and 12°S. Percentage of the explained variance for each mode are indicated. Values obtained by Belmadani et al. (2012) using the same method are also indicated.

	Sea level	17° C depth	20 $\mu$ M nitrate	Surface Chl
Propagation speed (m.s <sup>-1</sup> )	2.48 +/- 0.40	1.03 +/- 0.16	1.05 +/- 0.11	0.45 +/- 0.07
BC87 CTW mode	Barotropic/first	second	third	fourth
5° S mean (c, T)	3, 9-59, 8	2, 0-62, 6		
5° S mean	3, 9-59, 9	2, 0-60, 0	1, 2-60, 0	0, 6-59, 6
10° S mean	4, 3-65, 0	2, 0-70, 0		
10° S été	4, 3-60, 4	2, 0-60, 3	1, 2-59, 7	0, 6-61, 5
15° S mean	4, 3-58, 5	2, 1-60, 0		
15° S été	4, 3-60, 0	2, 1-60, 0	1, 2-60, 0	0, 6-60, 0
EOF Mode n°	1	2	3	
Variance at 8° S	42.8%	21.7%	11.7%	
Variance at 12° S	43.4%	26.4%	10.8%	
Maximum lag-correlation 8° S-12° S	0.53	0.14	0.29	
Propagation speed $c=\Delta L/\Delta T$	1,88 m/s	0,85 m/s	0,4 m/s	

**Vitesses estimées :**

2.48 +/- 0.40 m.s<sup>-1</sup> pour le niveau de la mer

1.03 +/- 0.16 m.s<sup>-1</sup> pour l'isotherme DT17° C

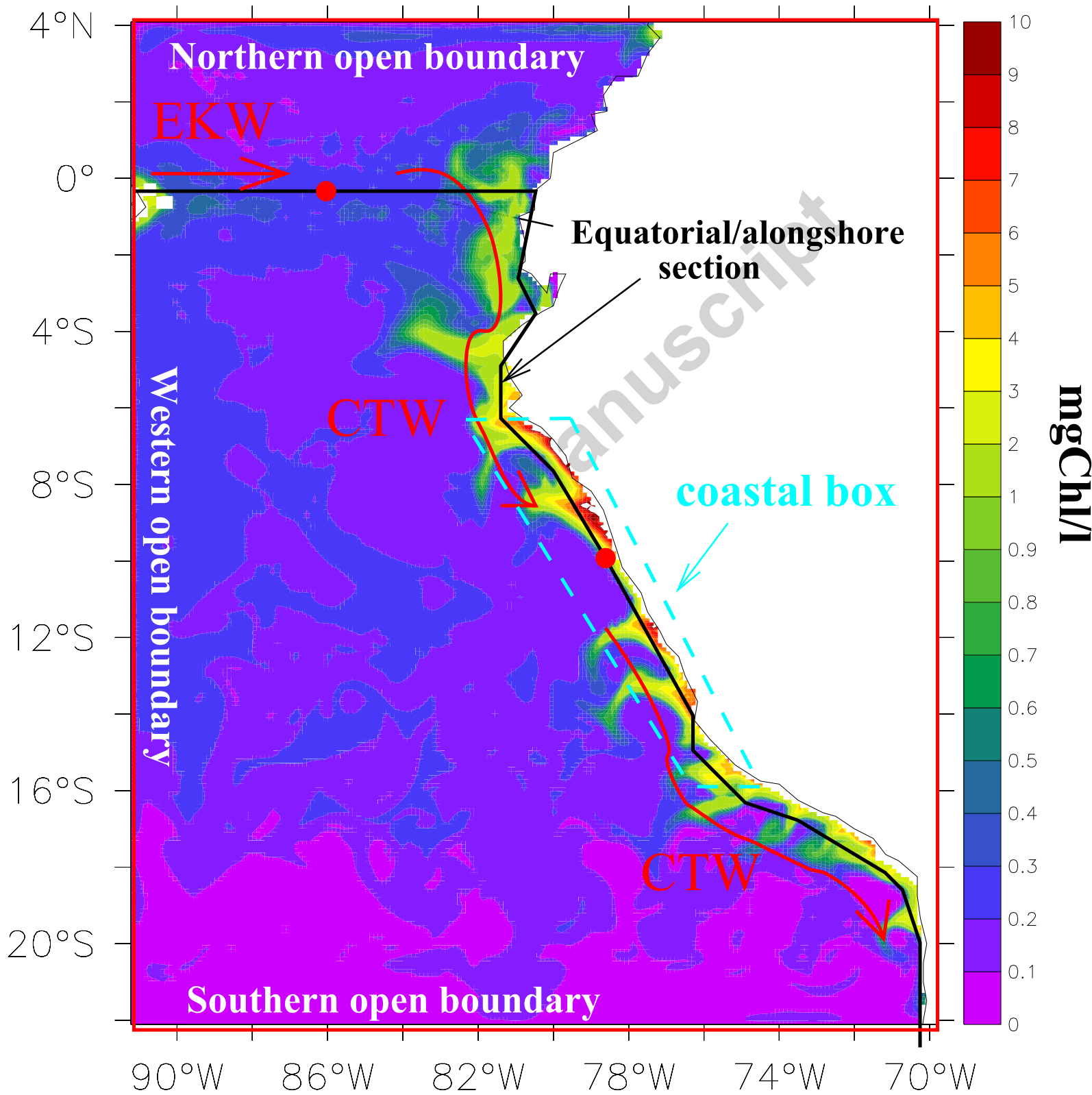
0.45 +/- 0.07 m.s<sup>-1</sup> pour la chloro

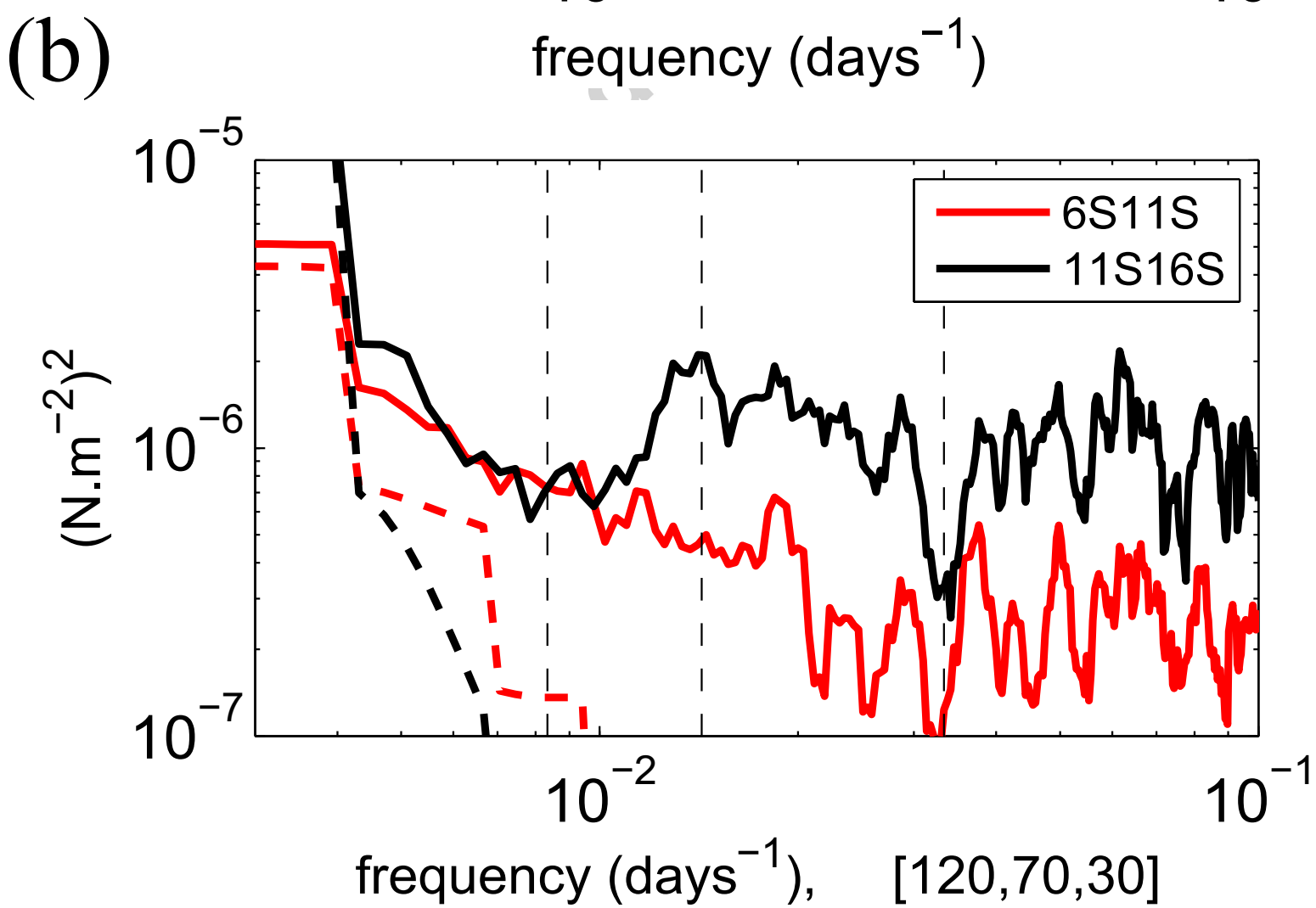
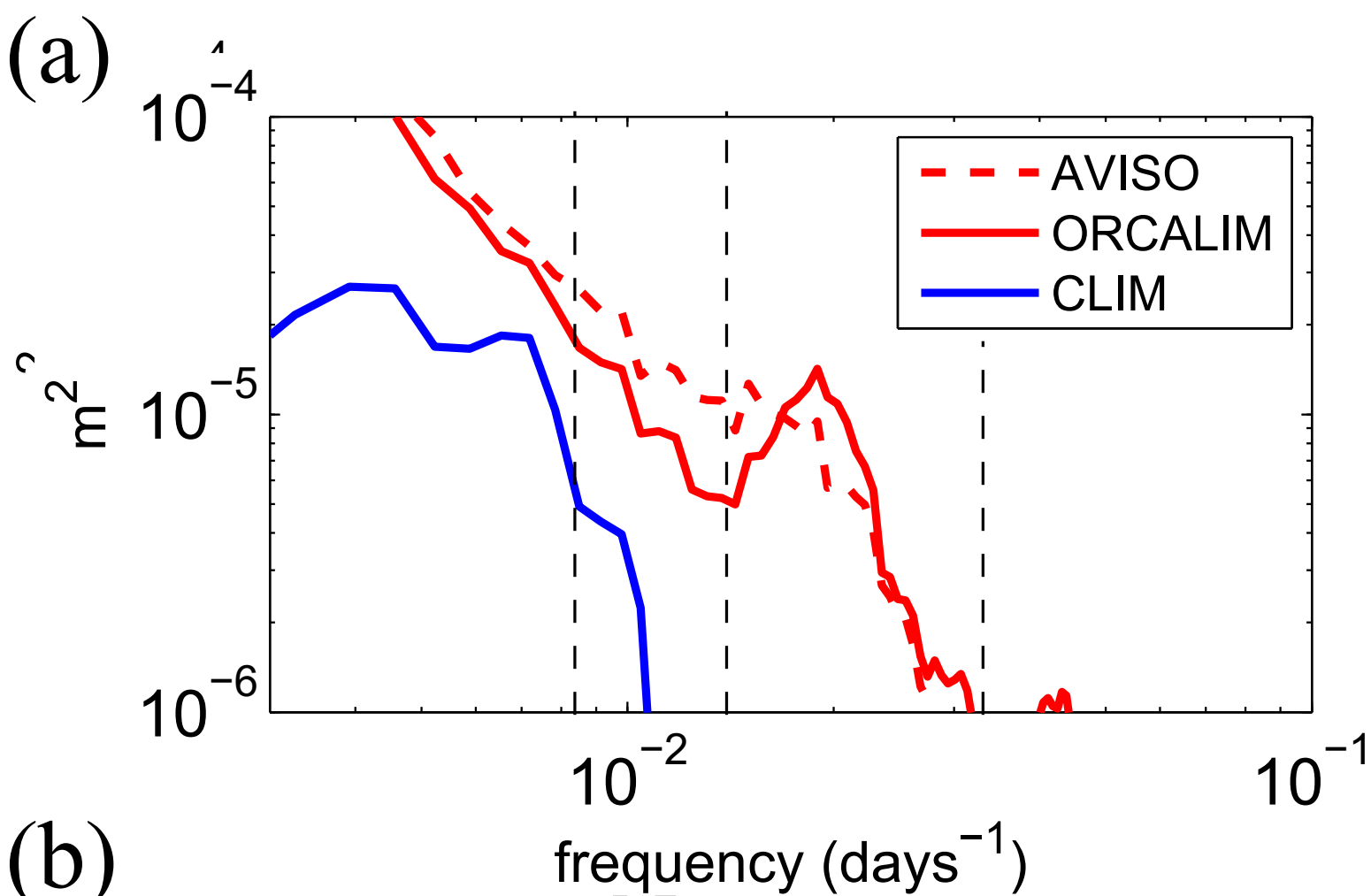
**Research highlights**

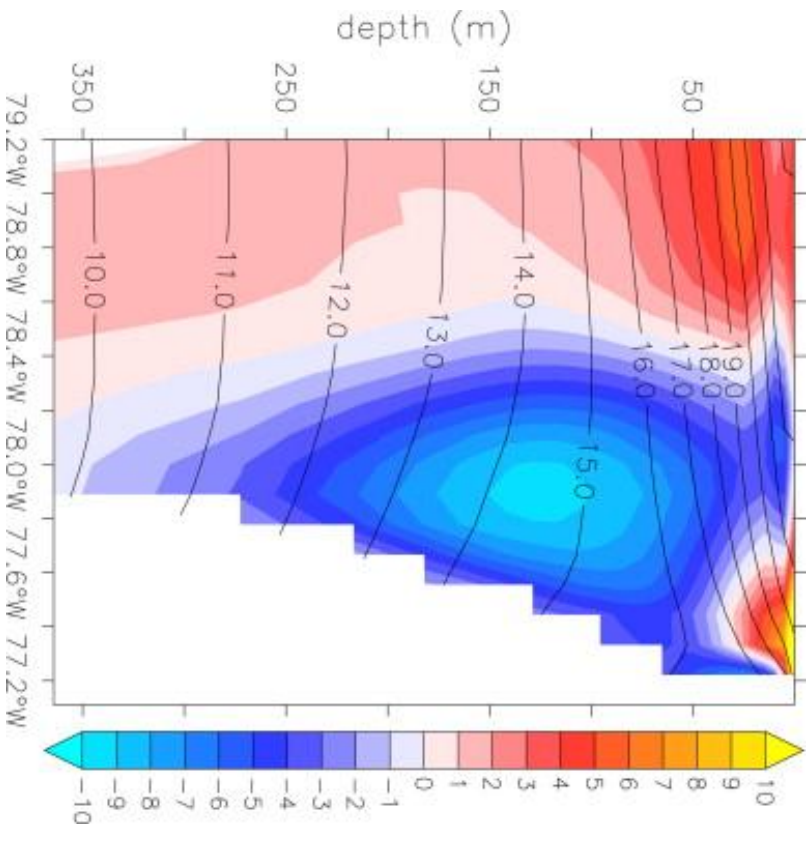
- Strong intraseasonal variability of near shore plankton in Peru upwelling system
- Chlorophyll variability is driven by the intraseasonal coastally trapped waves
- Chlorophyll anomalies propagate poleward at speed of high order CTW mode
- Intraseasonal wind impacts mainly the northern shelf variability and at 20-30 days

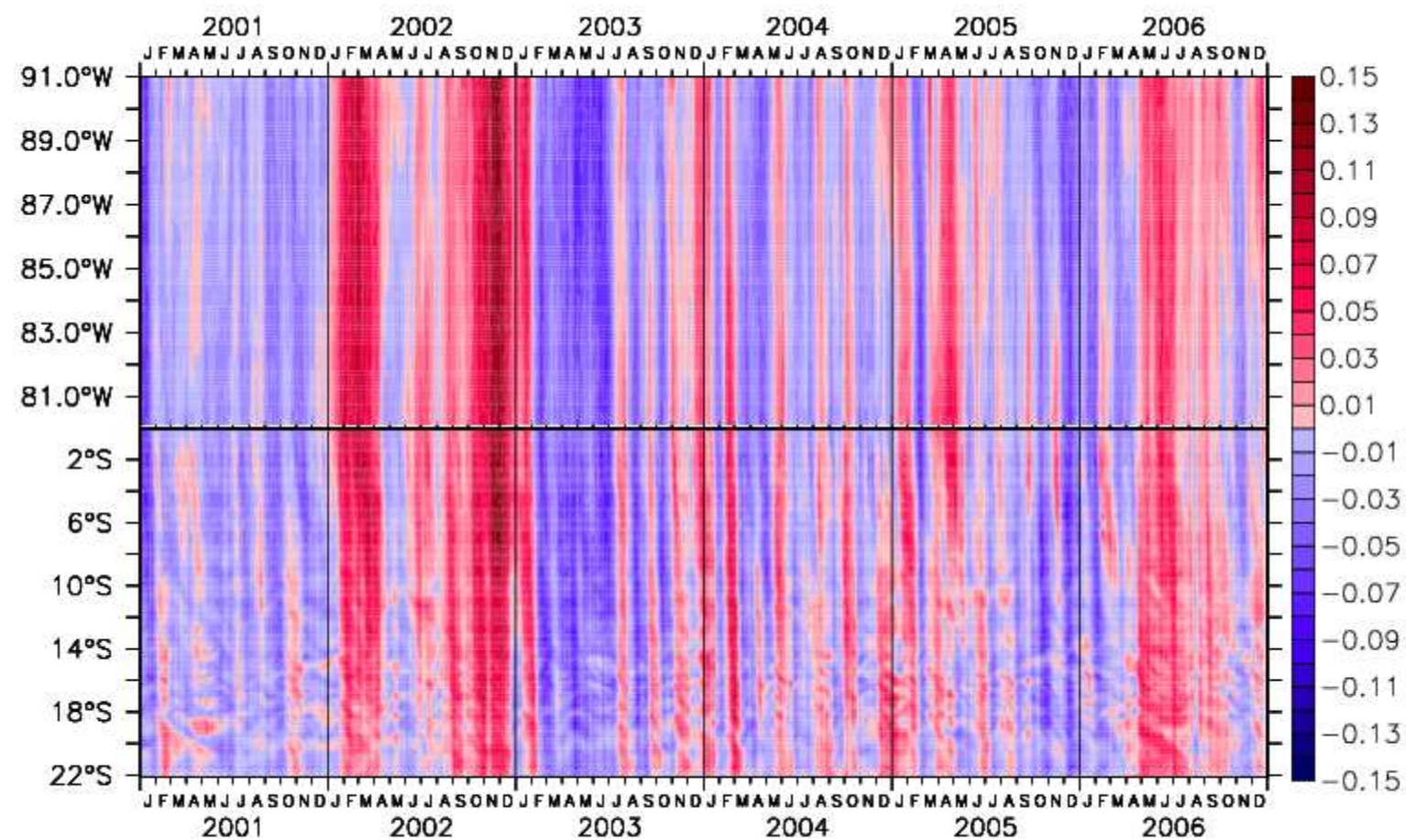
Accepted manuscript

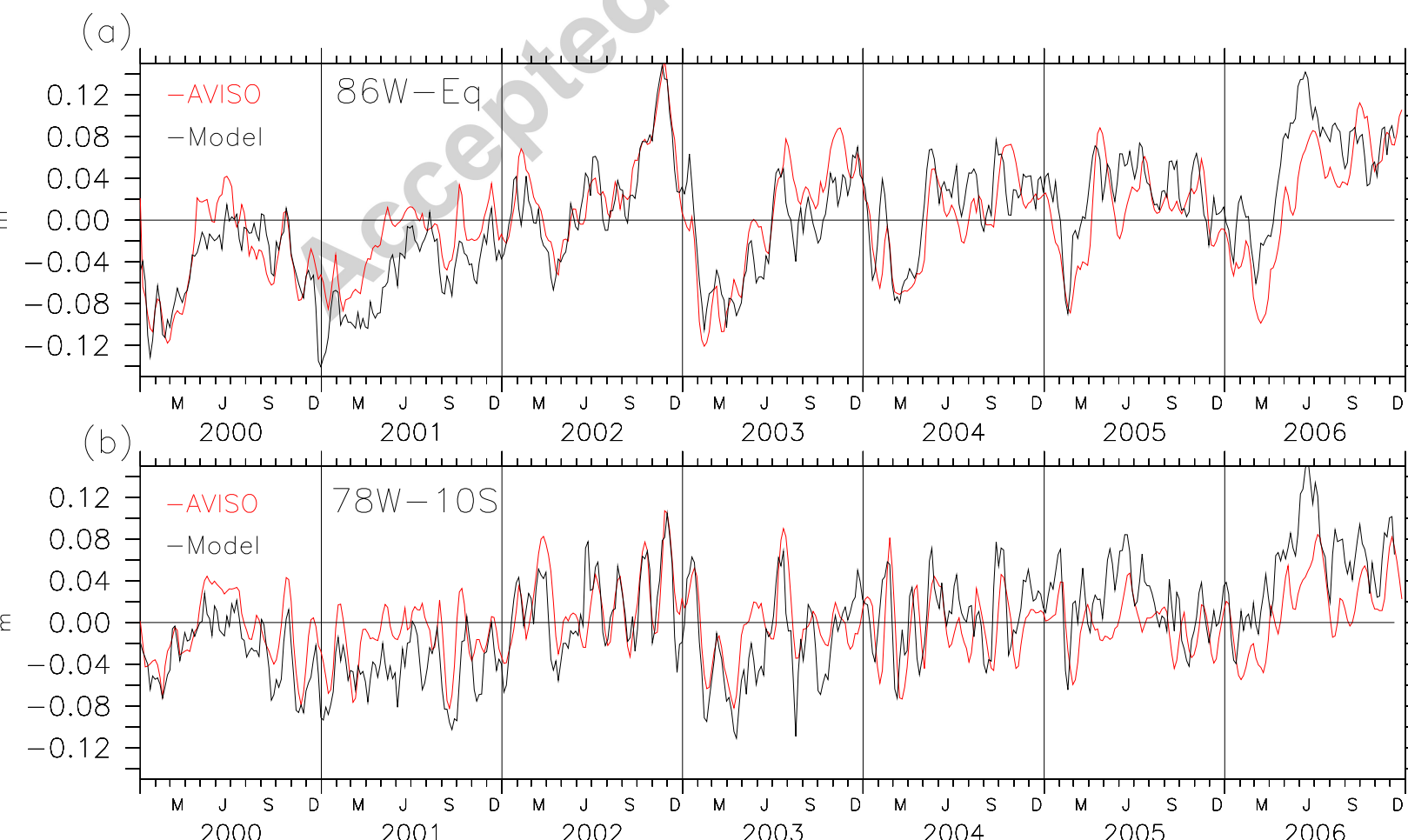
# ROMS domain

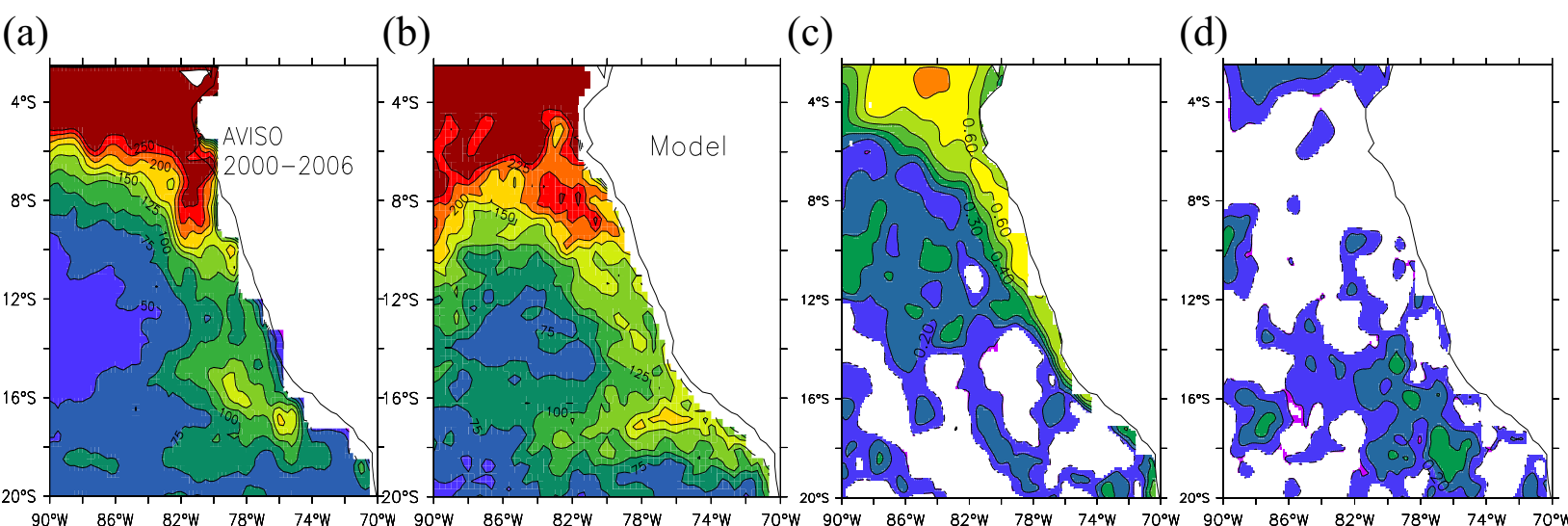


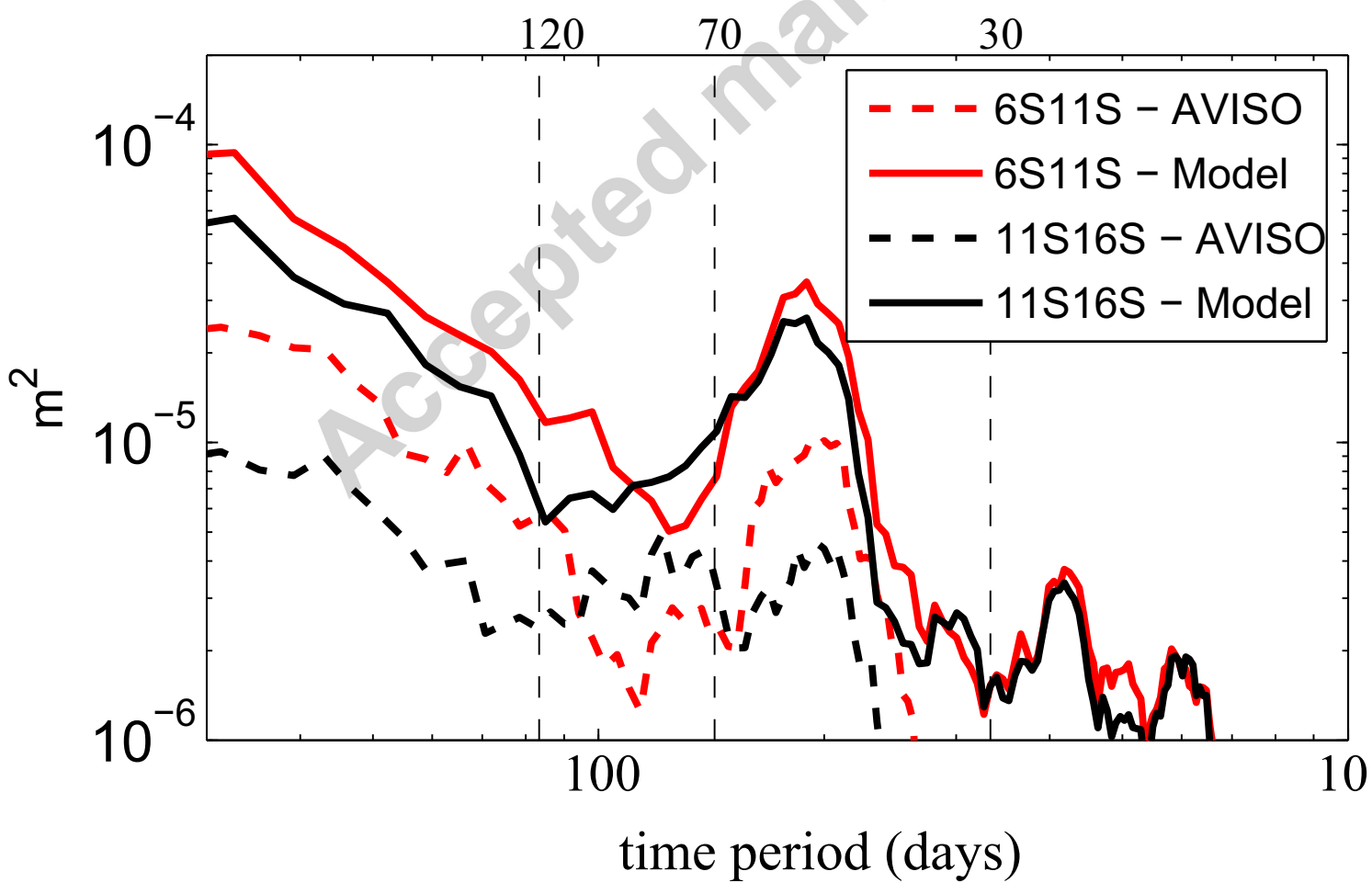


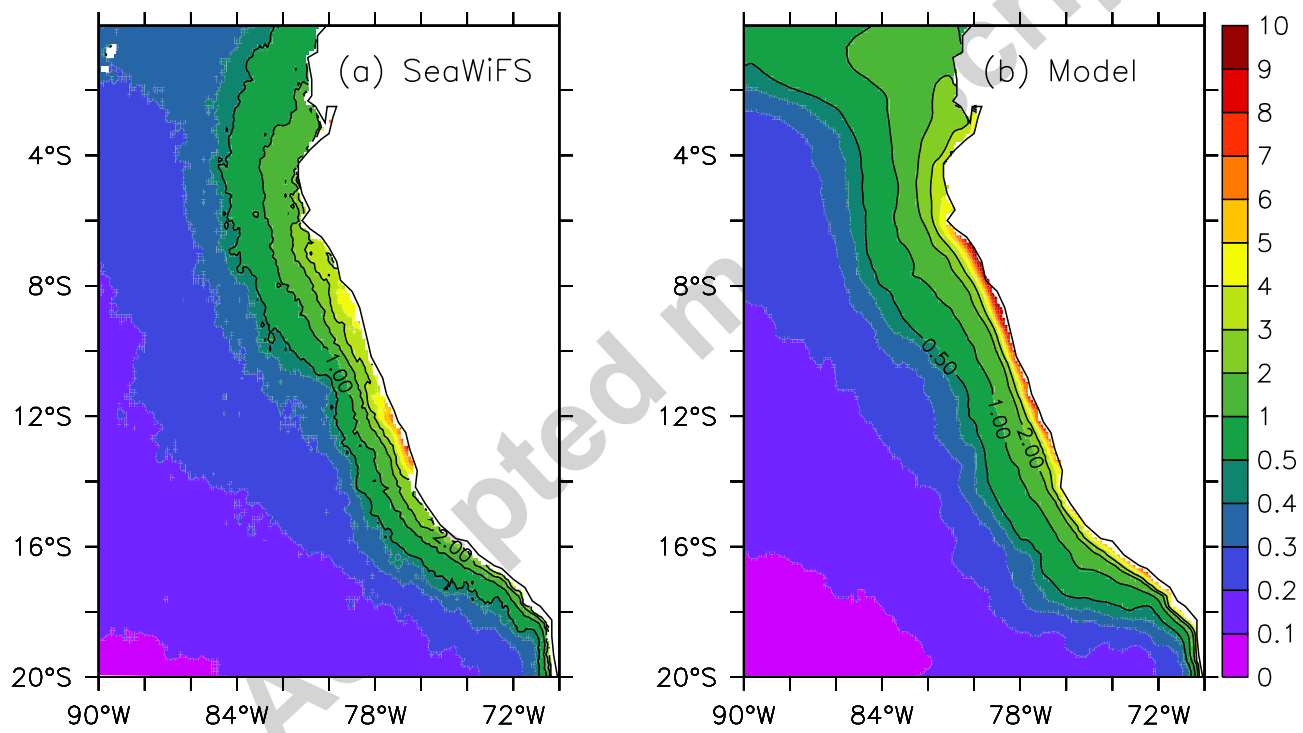


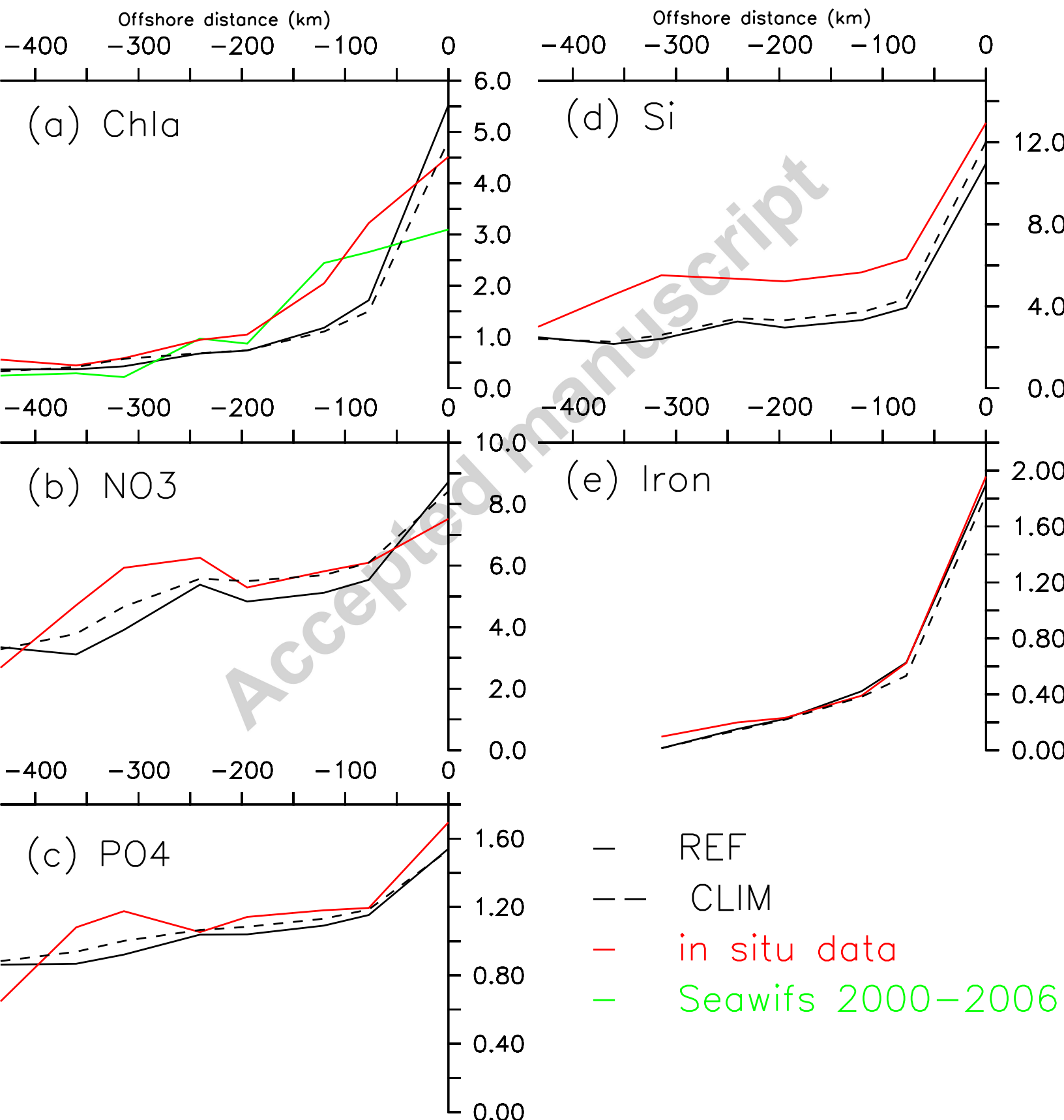


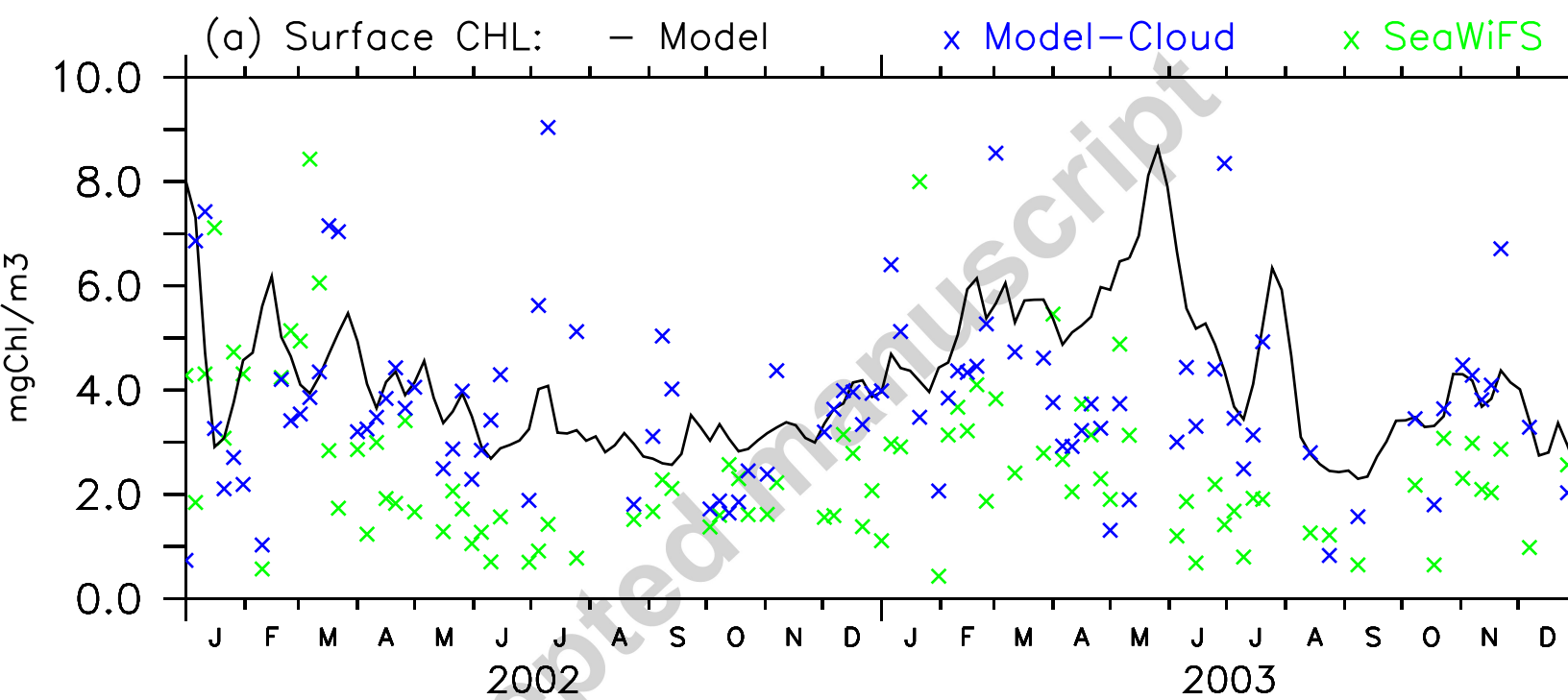




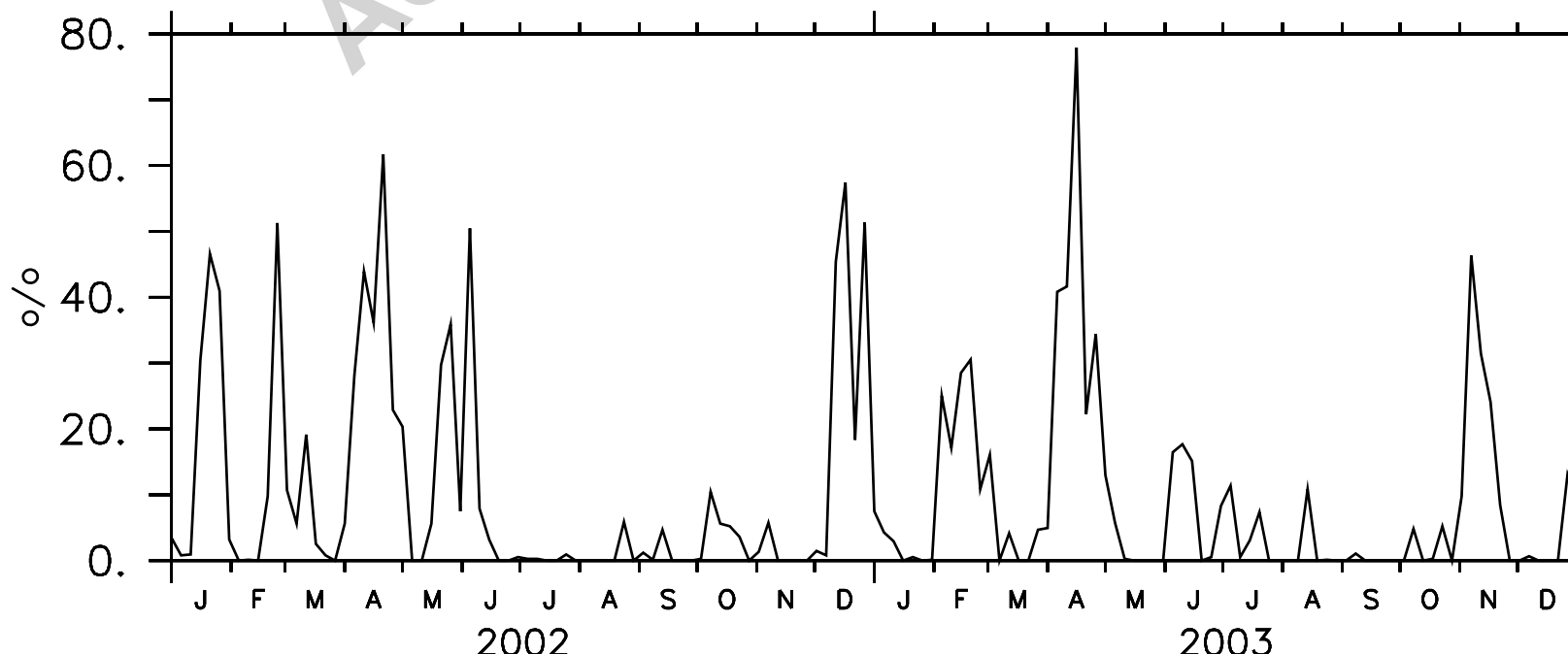


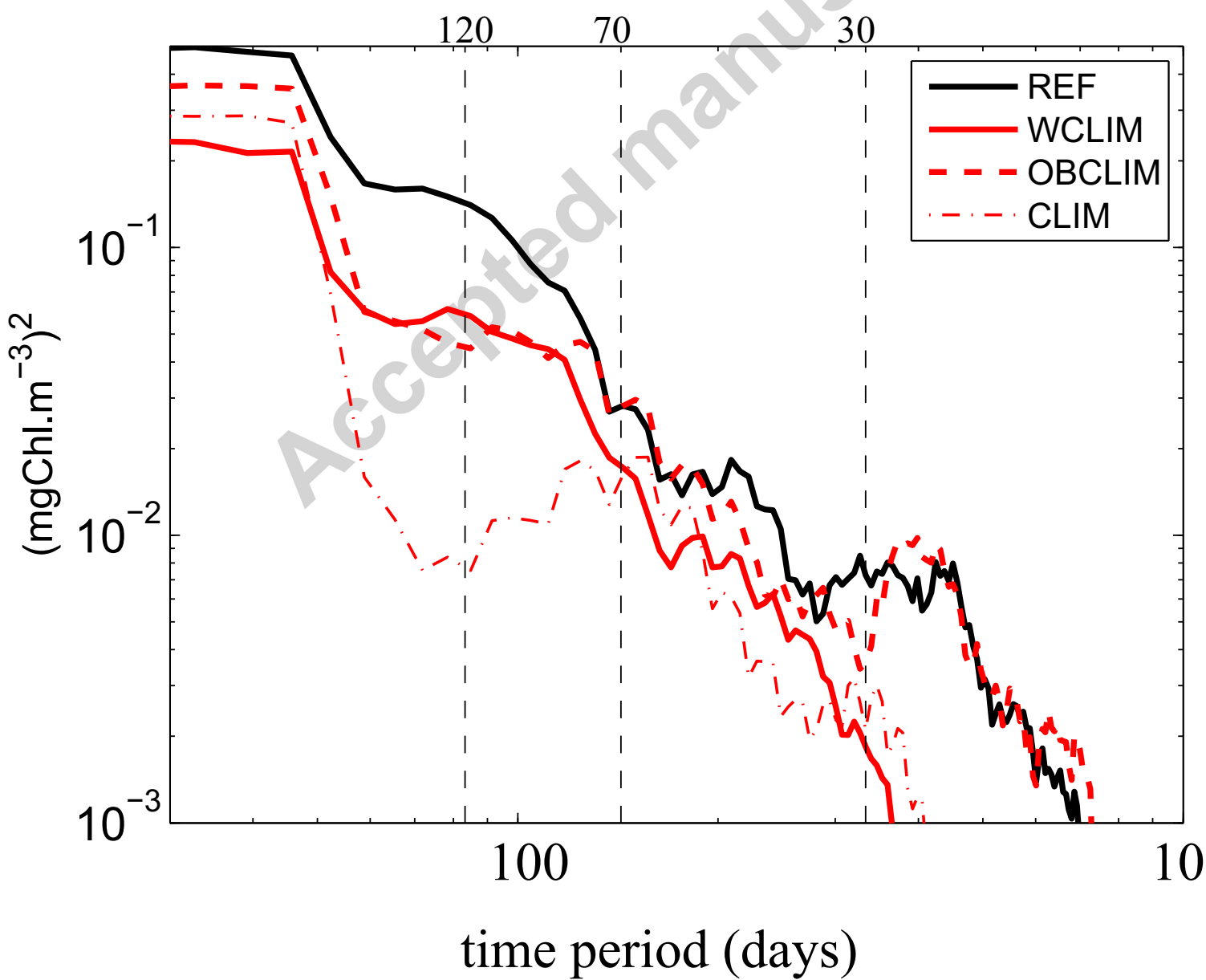


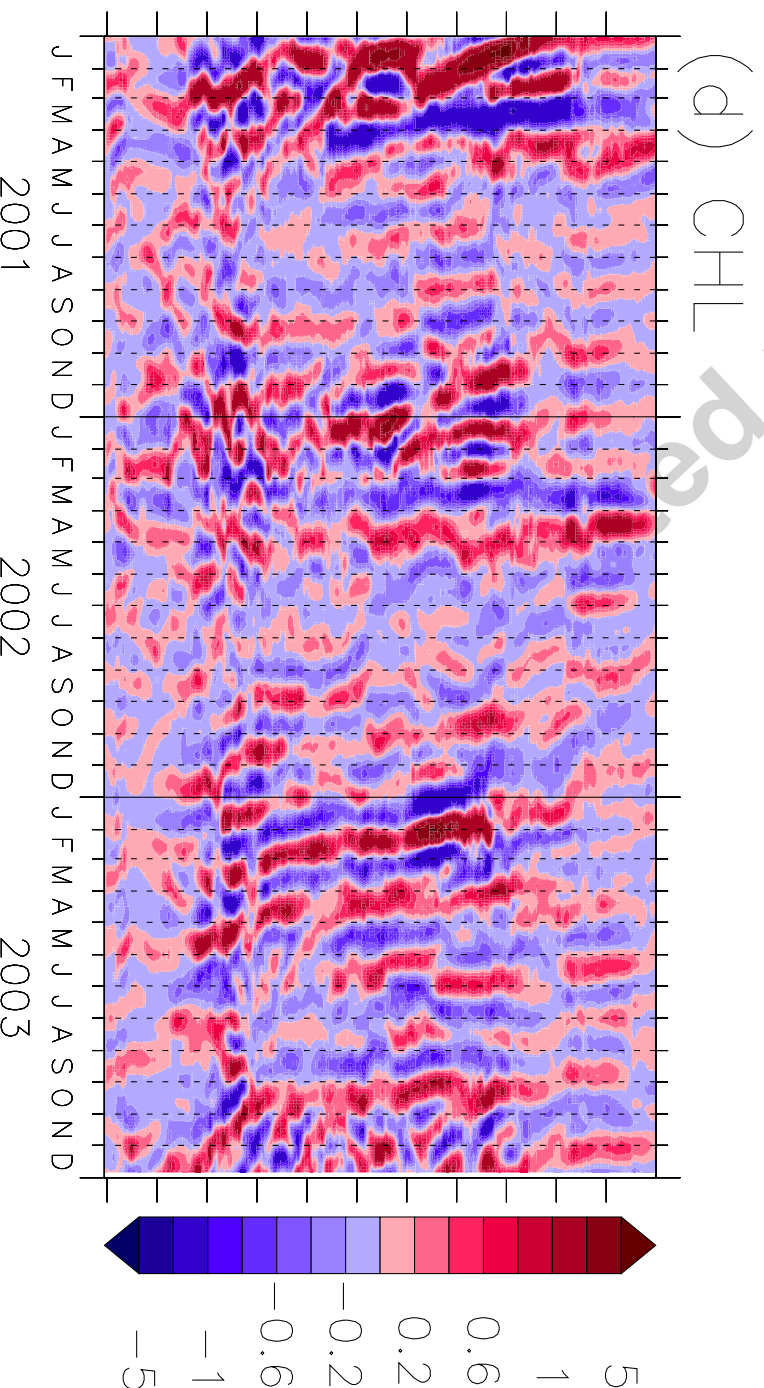
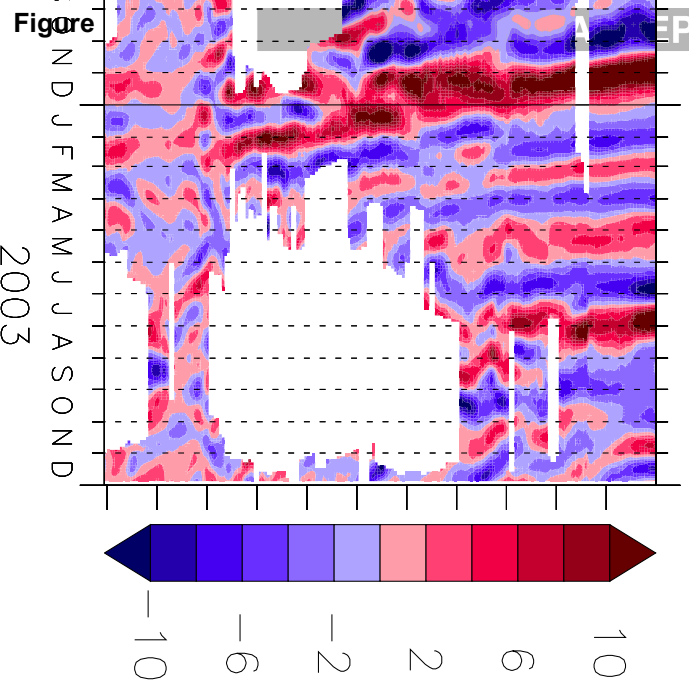
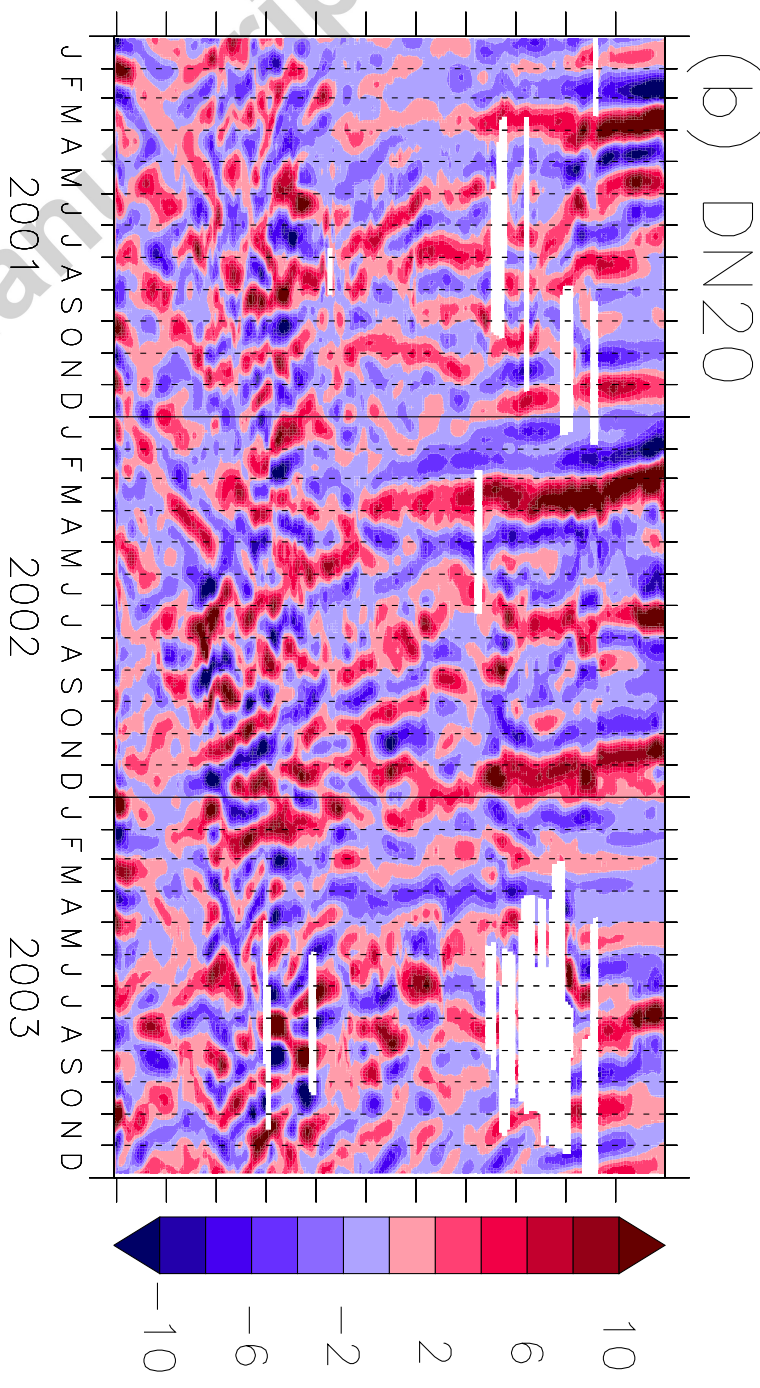
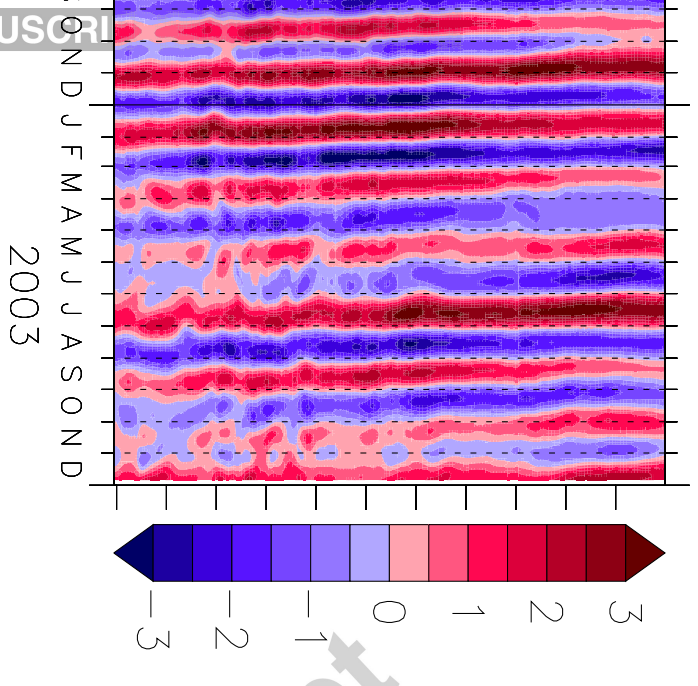


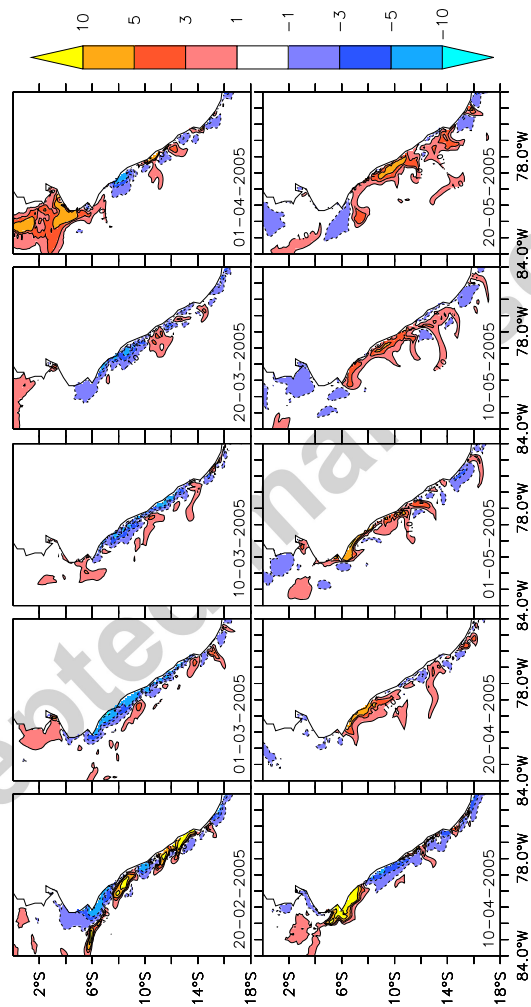


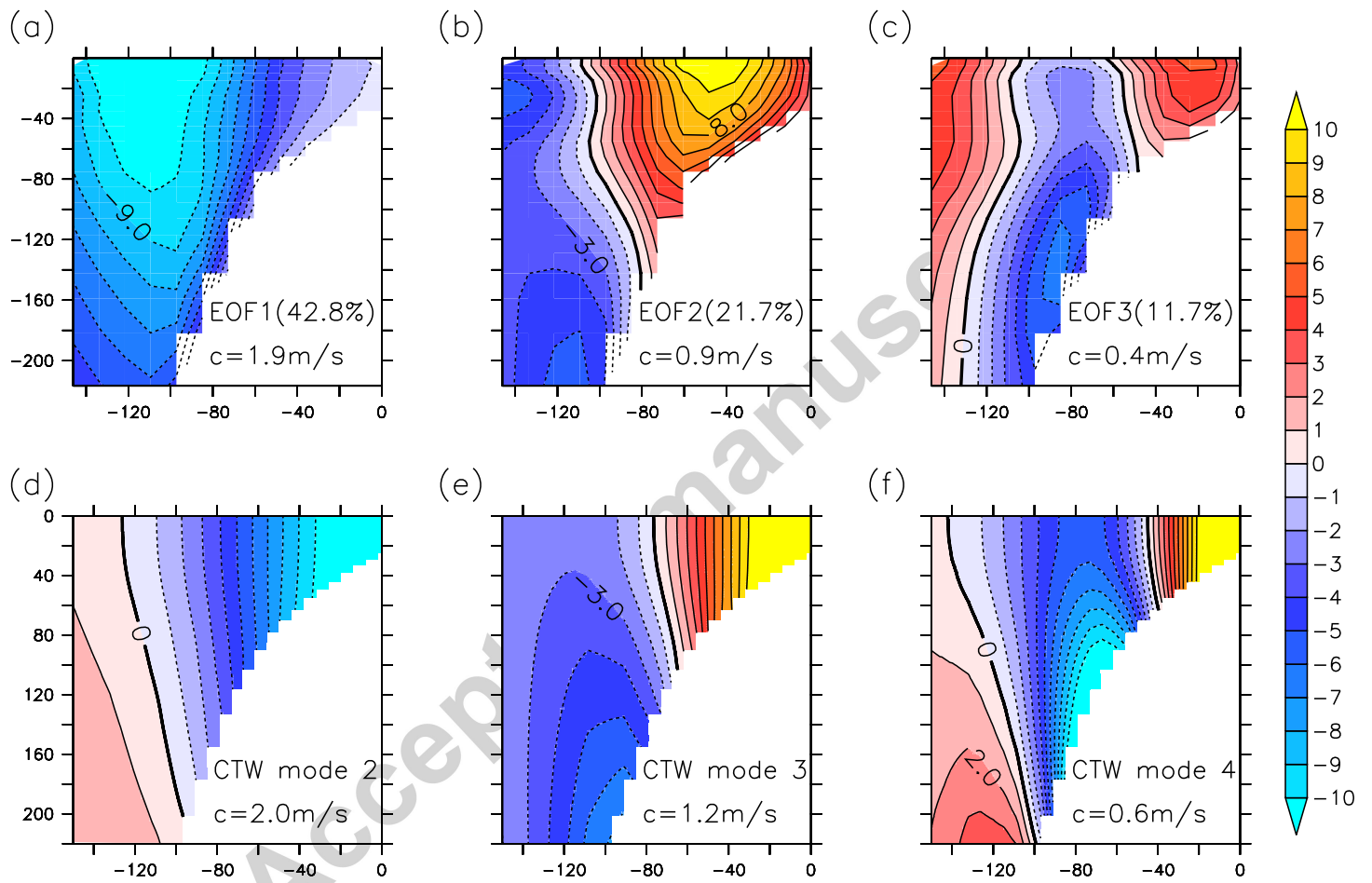
(b) Percentage of unflagged data

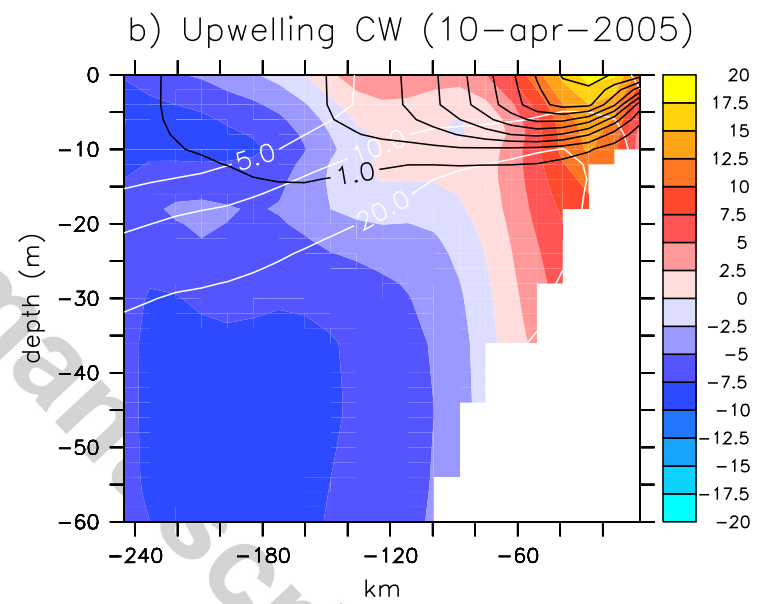
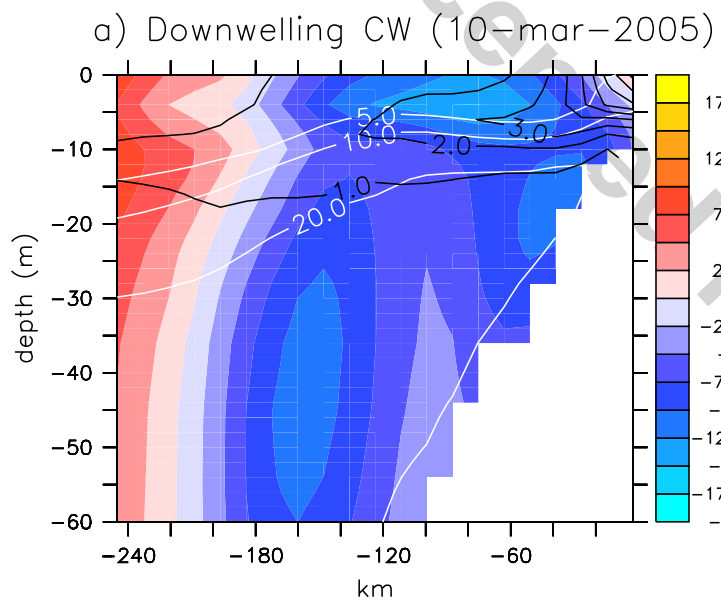


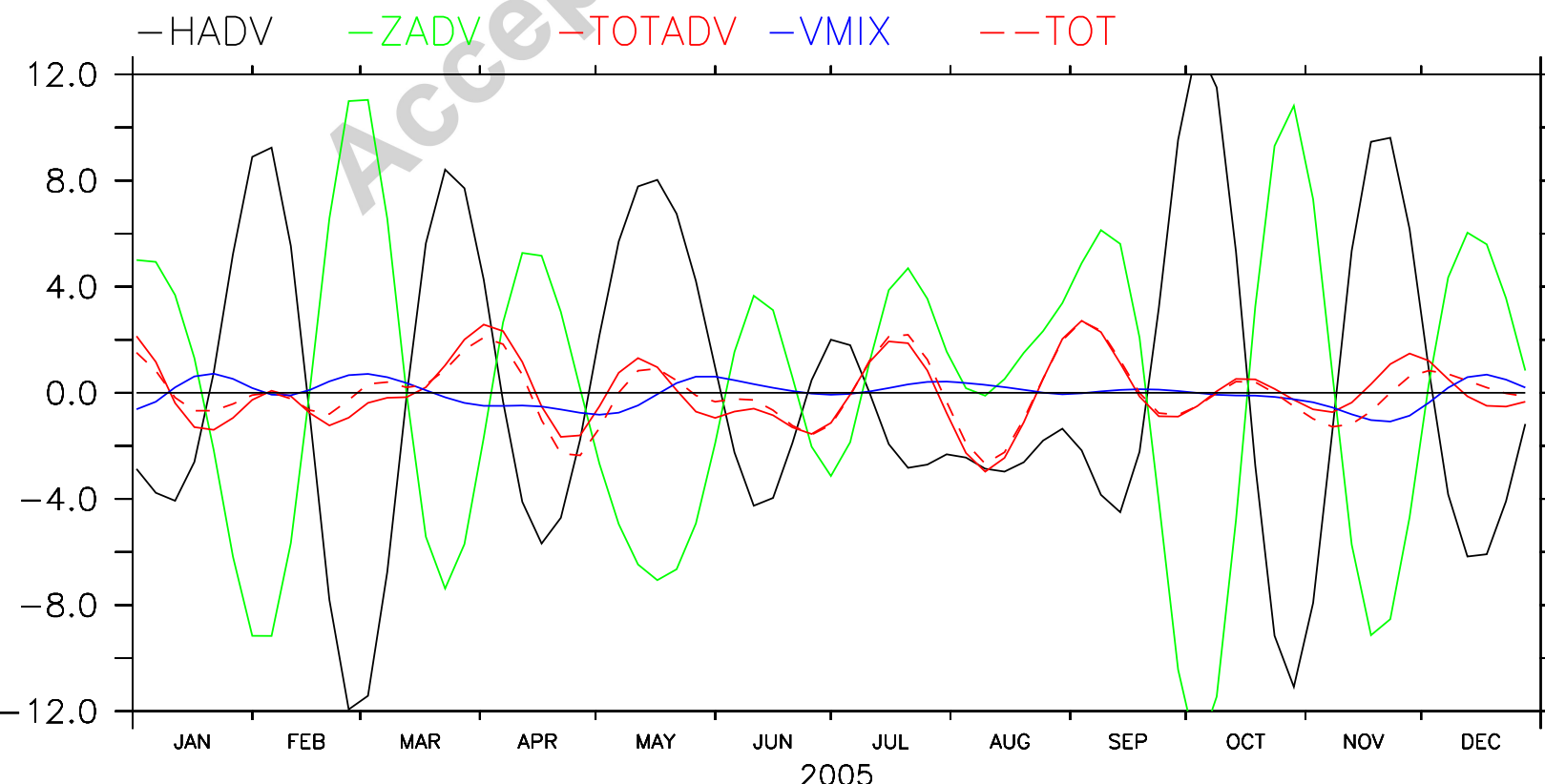












Figure

